

**High Resolution Radar Stratigraphy (GPR) of Braided Channel
Complexes in the Triassic Wolfville Formation- Controls on
Reservoir Heterogeneity**

Matthew J. Vaughan

Submitted in Partial Fulfillment of the Requirements
For the degree of Bachelor of Science, Honours
Department of Earth Sciences,
Dalhousie University, Halifax, Nova Scotia

April 2011

Distribution License

DalSpace requires agreement to this non-exclusive distribution license before your item can appear on DalSpace.

NON-EXCLUSIVE DISTRIBUTION LICENSE

You (the author(s) or copyright owner) grant to Dalhousie University the non-exclusive right to reproduce and distribute your submission worldwide in any medium.

You agree that Dalhousie University may, without changing the content, reformat the submission for the purpose of preservation.

You also agree that Dalhousie University may keep more than one copy of this submission for purposes of security, back-up and preservation.

You agree that the submission is your original work, and that you have the right to grant the rights contained in this license. You also agree that your submission does not, to the best of your knowledge, infringe upon anyone's copyright.

If the submission contains material for which you do not hold copyright, you agree that you have obtained the unrestricted permission of the copyright owner to grant Dalhousie University the rights required by this license, and that such third-party owned material is clearly identified and acknowledged within the text or content of the submission.

If the submission is based upon work that has been sponsored or supported by an agency or organization other than Dalhousie University, you assert that you have fulfilled any right of review or other obligations required by such contract or agreement.

Dalhousie University will clearly identify your name(s) as the author(s) or owner(s) of the submission, and will not make any alteration to the content of the files that you have submitted.

If you have questions regarding this license please contact the repository manager at dalspace@dal.ca.

Grant the distribution license by signing and dating below.

Name of signatory

Date



**DALHOUSIE
UNIVERSITY**

Inspiring Minds

Department of Earth Sciences

Halifax, Nova Scotia

Canada B3H 4J1

(902) 494-2358

FAX (902) 494-6889

DATE: April 25th, 2011

AUTHOR: Matthew James Vaughan

TITLE: High Resolution Radar Stratigraphy (GPR) of Braided
Channel Complexes in the Triassic Wolfville Formation -
Controls on Reservoir Heterogeneity

Degree: B.Sc Convocation: October Year: 2011

Permission is herewith granted to Dalhousie University to circulate and to have copied for non-commercial purposes, at its discretion, the above title upon the request of individuals or institutions.

Signature of ~~Author~~

THE AUTHOR RESERVES OTHER PUBLICATION RIGHTS, AND NEITHER THE THESIS NOR EXTENSIVE EXTRACTS FROM IT MAY BE PRINTED OR OTHERWISE REPRODUCED WITHOUT THE AUTHOR'S WRITTEN PERMISSION.

THE AUTHOR ATTESTS THAT PERMISSION HAS BEEN OBTAINED FOR THE USE OF ANY COPYRIGHTED MATERIAL APPEARING IN THIS THESIS (OTHER THAN BRIEF EXCERPTS REQUIRING ONLY PROPER ACKNOWLEDGEMENT IN SCHOLARLY WRITING) AND THAT ALL SUCH USE IS CLEARLY ACKNOWLEDGED.

Abstract

The Triassic Wolfville Formation crops out along the shoreline of the Minas Basin of the Bay of Fundy, Nova Scotia. Cambridge Cove contains an exceptionally well preserved outcrop which presents 2D and 3D exposures of the braided channel depositional environment of the Wolfville Formation. These outcrops demonstrate the stratigraphic complexities associated with the depositional environment.

This study uses Ground Penetrating Radar (GPR) survey techniques, spatially calibrated with Differential GPS (DGPS), to image braided channel depositional architecture in the subsurface for correlation to outcrop LiDAR. This provides 3D, hi-resolution stratigraphic and structural data about braided channel deposits and their characteristics as reservoirs. The data collected can be used to help us model fluid connectivity within braided channel complexes and the influence of these factors on hydrocarbon production and the potential for geologic sequestration of CO₂.

Post-processing methods have produced GPR profiles for interpretation. Radar facies have been recognized on lower frequency (50MHz) data, successfully imaging architectural and structural features (faults, a major unconformity and several stratigraphic horizons). Integration of these GPR grids into a 3D spatial framework with LiDAR data acquired from the outcrop adjacent to the survey location, has allowed for the comprehensive examination and delineation of the architectural elements of this braided channel deposit in 3D space. This architectural framework has been used to evaluate this deposit as hypothetical reservoir, exploring the nature of fluid connectivity and compartmentalization through the formation of baffles and barriers.

Table of Contents

Abstract	i
Table of Contents	ii
List of Figures	iii
List of Tables	iv
Table of Abbreviations	v
Table of Symbols	v
Acknowledgments	vi
1.0 INTRODUCTION AND BACKGROUND GEOLOGY	1
1.1 Study Area	1
1.2 Research Objectives	3
1.3 Thesis Organization	4
1.4 Fundy Basin Regional Geology	5
1.5 Depositional Environments and Geomorphology	8
1.5.1 Alluvial fan deposits and facies	9
1.5.2 Braided channel deposits and facies	11
1.5.3 Structural elements and geometries	15
2.0 METHODS	20
2.1 Introduction	20
2.2 Data Acquisition and Methodology	22
2.2.1 Differential GPS	23
2.2.2 Ground Penetrating Radar	25
2.3 Data Processing	38
2.4 LiDAR data	43
2.5 Construction of Digital 3D Environment	46
2.6 Mapping of GPR and LiDAR	53
3.0 RESULTS	54
3.1 Interpretation of GPR and LiDAR data	54
3.2 Sub-surface Structure Maps	58
4.0 DISCUSSION	63
4.1 Reservoir Characterization	63
4.2 Methodology Recommendations	68
5.0 CONCLUSIONS	70
6.0 REFERENCES	71
Appendix A: Trim-shift SEG Y Programming	73

List of Figures

1.1	Simplified geological map of Nova Scotia including location of the Minas sub-basin	1
1.2	Google Earth image of the Minas sub-basin	2
1.3	Aerial view of Cambridge Cove and the Minas View Golf Course	2
1.4	Unconformity between Carboniferous shale and overlying Triassic sandstone	5
1.5	Sediments of the Fundy basin and the other Mesozoic syn-rift basins	6
1.6	Fundy-type basin geometry analog	7
1.7	Depositional model for the margins of Minas basin and the Wolfville formation	9
1.8	Image of modern analog to braided channel complexes of the Wolfville formation	10
1.9	3D exposure of a preserved braided channel barform in the intertidal zone	12
1.10	Bedload deposits of a braided river system	13
1.11	Coarse, lithic, pebbly sandstones	13
1.12	Classic isolated block at Cambridge Cove displaying complex internal geometries	14
1.13	A modern alluvial fan viewed from space	15
1.14	Terminology for describing cross sectional geometry of multi-story channel bodies	16
1.15	Terminology for describing the three dimensional form of channel bodies	17
1.16	Normal faults in the 15m high cliff section at Cambridge Cove	18
1.17	Measured section 5 location	19
2.1	Aerial view of study areas where GPR data was acquired as X-Y grids	23
2.2	Leica 1200 DGPS base station, radio transmitter and antenna	25
2.3	GPR cart	26
2.4	Common offset survey geometry	27
2.5	GPR ray path geometries	28
2.6	Frequency dependence of resolution and penetration depth	33
2.7	Convolution of EM wave with subsurface electrical impedance	34
2.8	GPR elliptical footprint approximation	34
2.9	Generation of diffractions	35
2.10	Bowtie anomalies, dip errors, diffraction examples	36
2.11	GPR data preliminary steps	38
2.12	Amplitude vs. time, Amplitude vs. frequency	39
2.13	Processing window in EKKO_View Deluxe	40
2.14	Processing workflow diagram	41
2.15	Raw vs. processed GPR profiles	42
2.16	Optech LiDAR imaging system at Joggins	43
2.17	LiDAR shot location and raw LiDAR data	45
2.18	LiDAR image characterized by intensity in Petrel 2010	47
2.19	UTM coordinates before and after linear interpolation	49
2.20	3D construct workflow diagram	50
2.21	2D GPR grid survey, UTM coordinates for survey lines	51
2.22	Final 3D construct	52
2.23	Example of horizon mapping and digitization	52

3.1	Mapped horizons on LiDAR data with outcrop photograph and measured section	52
3.2	Measured section 5	53
3.3	Matrix-supported conglomerate	54
3.4	Radar facies 1, Radar facies 2, Radar facies 3	56
3.5	Representative GPR profile with interpretations	57
3.6	GROUND horizon	58
3.7	Top Unit 2 horizon	58
3.8	Top Unit 1 horizon	59
3.9	Fault L map	59
3.10	Unit 2 Architecture map	61
3.11	Complete 3D subsurface map	62
4.1	Braided channel geometry superimposed on annotated Cycle 2 Architecture map	64
4.2	Lithofacies mapped to outcrop and LiDAR	65

Tables

Abbreviations	v
Symbols	v
Facies characteristics	56
Lithofacies permeability values	66

Table of Abbreviations

GPR: Ground Penetrating Radar
GPS: Global Positioning System
DGPS: Differential Global Positioning System
LiDAR: Light Detecting and Ranging
UTM: Universal Transverse-Mercator coordinate system
2D: Two dimensional
3D: Three dimensional
TWT: Two-way travel time
NMO: Normal Moveout

Table of Symbols

Dielectric permeability (ϵ)
Electrical conductivity (σ)
Magnetic permeability (μ)
Electromagnetic wave velocity in a vacuum (c_0)
Angular frequency (ω)
Attenuation constant (α)
Amplitude (A)
Initial Amplitude (A_0)
Reflection Coefficient (R)
Velocities of adjacent layers 1 and 2 (V_1, V_2)
Wavelength (λ)
Velocity (v)
Frequency (f)
Depth (z)

Acknowledgements

First and foremost, I would like to thank my supervisor Grant Wach for his support and assistance throughout the completion of this thesis. Without his efforts of behalf of Dalhousie students, the sophisticated equipment required to complete this research would not otherwise have been available. I would like to thank Tom Duffett, Darragh O'Connor, Christian Rafuse, Johnathan Thibodeau, Kyle Landry, Fergus Tweedale and Hayley Pothier for their strong backs and assistance in completing the field work portion of this project. I would like to give further recognition to Johnathan Thibodeau, Joanna Gerlings, Paul Mattern and Keith Loudon for their consistent and enthusiastic assistance in resolving numerous geotechnical issues and tireless programming efforts. Without their advanced knowledge of programming and seismic imaging, the primary construct of this thesis would never have materialized. I would like to thank Lawrence Plug for training me in the use of his DGPS equipment and for making it available for use in the field. For funding of this project and my attendance at several conferences throughout this last school year, I would like to thank Shell Canada for their generosity.

CHAPTER 1: INTRODUCTION AND BACKGROUND GEOLOGY

1.1 Study Area

Cambridge Cove is located along the southern margin of the Minas sub-basin of the larger Fundy Basin of Nova Scotia (Fig. 1.1). Located 99 km from Halifax, the beachfront outcrops of Cambridge Cove lie 25 km to the north east of the town of Wolfville, Nova Scotia in the Walton district (Fig. 1.2). The outcrops are excellent, extensive cliff face exposures of a major angular unconformity where fluvial and aeolian facies of the mid to late Triassic Wolfville Formation overlies strata of the Early Carboniferous Horton Bluff Formation.

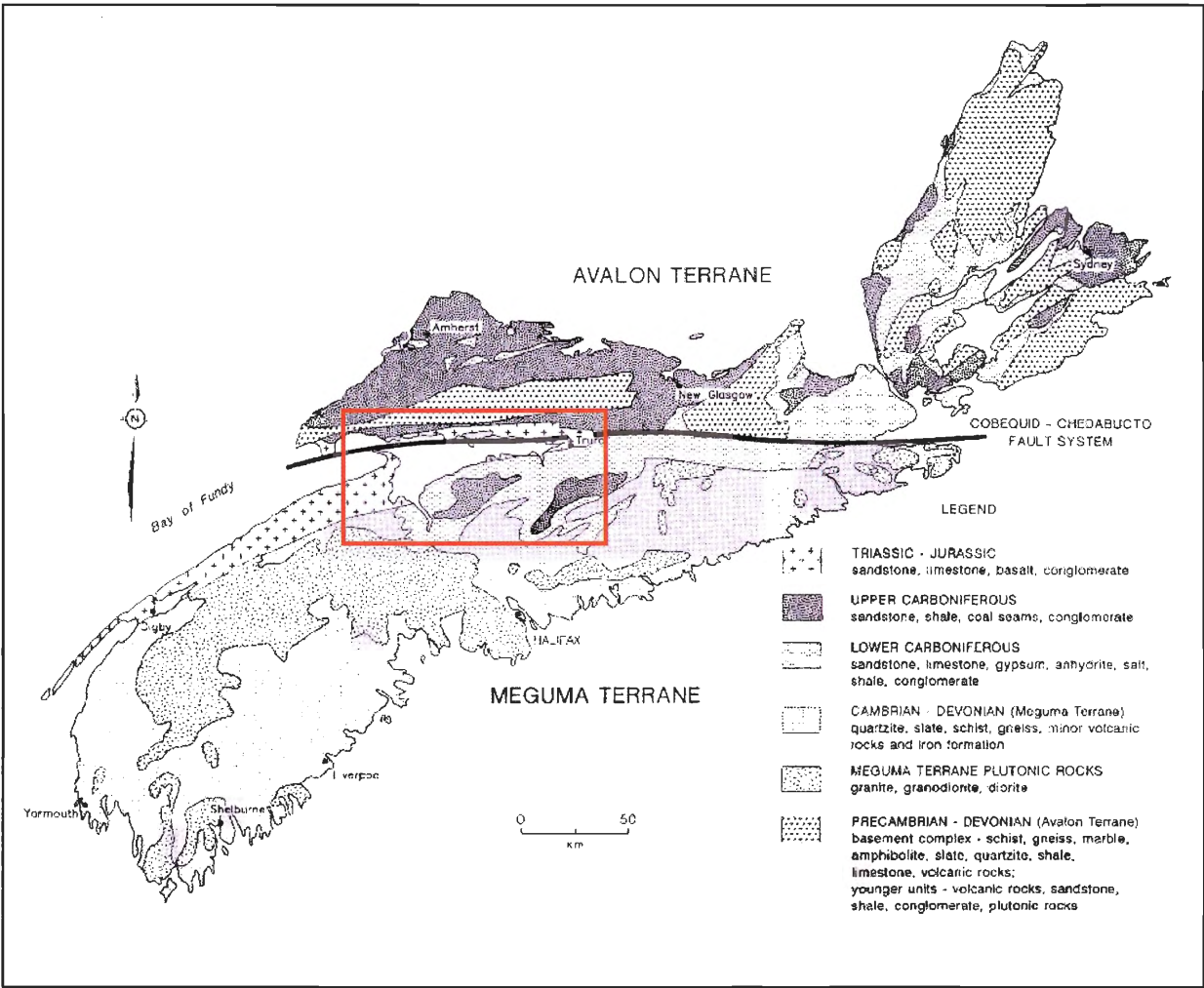


Figure 1.1: Simplified geological map of Nova Scotia indicating the location of the Minas Sub-Basin (NSDNR 2010).



Figure 1.2: Google Earth image of the Minas sub-basin indicating the Walton district where Cambridge Cove is located.



Figure 1.3: Aerial view of Cambridge Cove and the Minas View golf course where field research was conducted.

This section contains an exceptionally well preserved outcrop with 2D and 3D exposures of the braided channel depositional environment of the Wolfville Formation. The complexities of stratigraphic and architectural relationships of braided channel systems can be observed in several locations along the outcrop. Near-surface geophysical methods of defining these geometries in further detail are explored in this thesis.

1.2 Research Objectives:

Over the past several decades, studies of ancient and modern fluvial channel deposits have focused largely on their internal organisation, identifying architectural elements and bounding surfaces, emphasizing internal heterogeneities that control fluid flow through channel fills (Gibling 2006) in a 2-Dimensional framework. In contrast, few have dealt comprehensively with the dimensions and 3D-form of channel deposits and valley fills. Such information is important for several reasons.

The application of stratigraphy requires a strong understanding of the dimensions and scale of fluvial channel bodies because alluvial landscapes may respond rapidly to changes in factors such as base-level change, climate, lateral confinement, relief, or sedimentary input. Fluvial channel deposits form reservoirs, host economic minerals and important-fossil rich deposits. 3D seismic surveys are providing remarkable subsurface images of channel bodies and their morphological characteristics. One primary goal in this study is to test the application of Ground Penetrating Radar methodology to provide hi-resolution subsurface profiles similar to those produced by seismic methods.

The complexity of the braided channel deposit architecture displayed at Cambridge Cove (Fig. 1.3) is impossible to understand in a 3-Dimensional context based on outcrop observations alone. The aim of this study is to employ shallow subsurface geophysical methods in the field to

study the Wolfville Formation braided channel deposits in a more comprehensive spatial framework. This study will use ground penetrating radar (GPR) for subsurface imaging, differential Global positioning systems (DGPS) and Light Detection and Ranging (LiDAR) point cloud imaging data for mapping outcrop geometries and stratal packages. The study area presents the perfect environment for the acquisition of GPR data. The Minas View golf course, a region void of any significant surface obstacles, is situated immediately above and behind the outcrop of interest along an extensive portion of the section. This layout represents an excellent opportunity to gather subsurface data and correlate the mapped structures to features observable in the adjacent outcrop.

This study aims to construct a 3D spatial framework that can be used to describe the architecture of the Wolfville braided channel deposit in a GPR data environment for direct correlation to outcrop LiDAR available from Nickerson (2010). Once described, the nature of the deposits architectural heterogeneities will be considered for their influence on a hypothetical reservoir.

1.3 Thesis Organization:

This thesis will outline the essential geology of the Fundy Basin and construct a framework for understanding the fundamentals of braided channel systems and their morphological and sedimentological characteristics. The methods sections will outline the principles of GPR and LiDAR geophysical techniques, how and why they have been applied in the field and the parameters for using these methods to examine a braided channel complex. The results section will detail the construction of a digital 3D environment to make observations about the deposit and what geological observations have been derived from this comprehensive

spatial construct. The discussion section will explore the implications of both methodologies and subsequent observations with application to reservoir systems.

1.4 Fundy Basin Regional Geology:

The Fundy Basin forms one of a series of early Mesozoic rifts developed along the northwestern Atlantic margin and can be characterized by two principle stages of deformation: (1) synsedimentary extension from middle or early Late Triassic to early Jurassic and (2) basin inversion from early Jurassic to early Cretaceous (Leleu et al. 2009). The Carboniferous saw intensive tectonic activity in this area following the Devonian Acadian orogeny. Uplift and subsidence events lead to the cyclical deposition of continental, marine (Early Carboniferous Horton and Windsor Groups) and fluvial sediment bodies (Mabou, Cumberland and Pictou groups of the late Carboniferous) (Wach 2009).

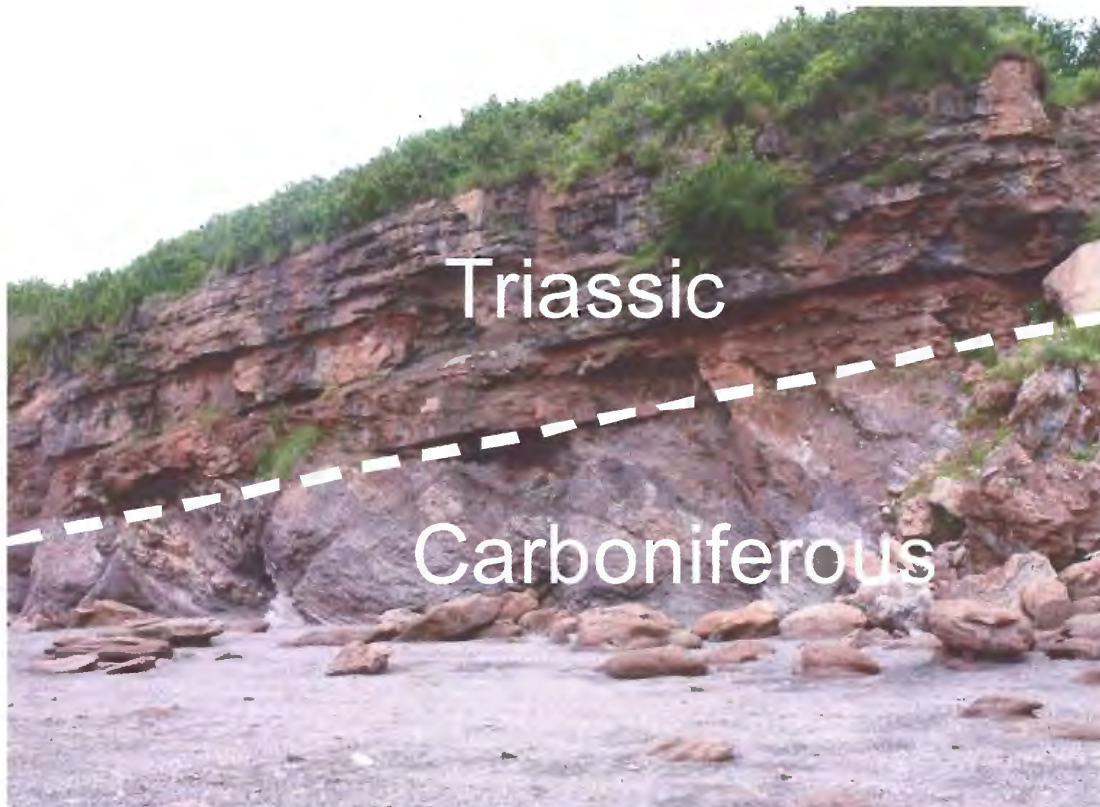


Figure 1.4: Unconformity between underlying Carboniferous Horton Group shales and overlying Triassic Wolfville Formation sandstones at Cambridge Cove.

This orogenic activity was followed by the onset of the breakup of Pangea in the Mesozoic and the rifting and drifting that led to the development of the Atlantic Ocean. The Fundy Basin is a remnant of the failed attempt to split Africa from North America, after which rifting shifted and continued to the southeast, leading to the development of the modern Atlantic Ocean. During the mid-Atlantic rifting event, several rift basins developed which contain sedimentary and volcanic rocks that are genetically similar to those of the Fundy Basin. Collectively they are named the Newark Supergroup. Figure 1.5 demonstrates the correlation of these basins (Olsen 1990). The Triassic Wolfville Formation within the Mesozoic strata of the Fundy Group lies unconformably above Carboniferous and older strata of the Horton Group (Figure 1.4).

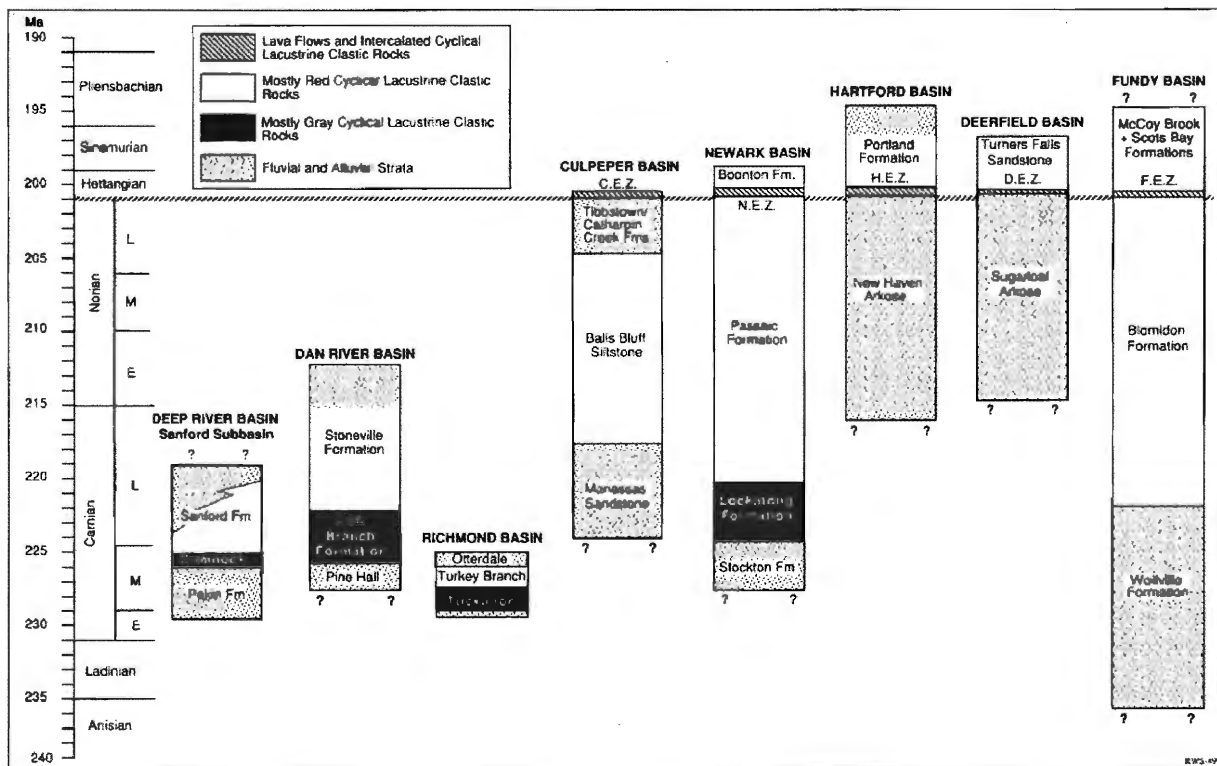


Figure 1.5: Correlation and facies types in the Newark Supergroup Basins modified from Olsen 1990. (CEZ, Culpeper basin extrusive zone; NEZ, Newark basin extrusive zone; HEZ, Hartford basin extrusive zone; DEZ, Deerfield basin extrusive zone; FEZ, Fundy basin extrusive zone).

These Mesozoic and Carboniferous units are both situated above the accreted igneous and metasedimentary basement terranes of the Avalon to the north and Meguma to the south. These two terranes are separated by the Cobequid – Chedabucto fault system which was reactivated during the Mesozoic and underwent oblique-slip movement, causing the Minas Basin to extend laterally into the heart of modern day Nova Scotia (Wade et al. 1996).

During this initial spreading, a rift basin began to develop that would host the sedimentary deposits of the Wolfville Formation and other rocks of the Fundy Group that we see today. As the Fundy basin began to expand, rifting and subsidence instigated basin filling in the form of fluvial and alluvial sediments of the early Triassic Wolfville Formation, and lacustrine sediments of the late Triassic Blomidon Formation.

Today, the Fundy rift basin (Fig. 1.6) takes shape as a southwest plunging synformal half graben that thickens in the same direction and extends as far south as Grand Manan Island. This configuration is likely controlled by fault reactivation along the northern edge of the Minas sub-basin with normal and strike-slip components (Olsen 1990).

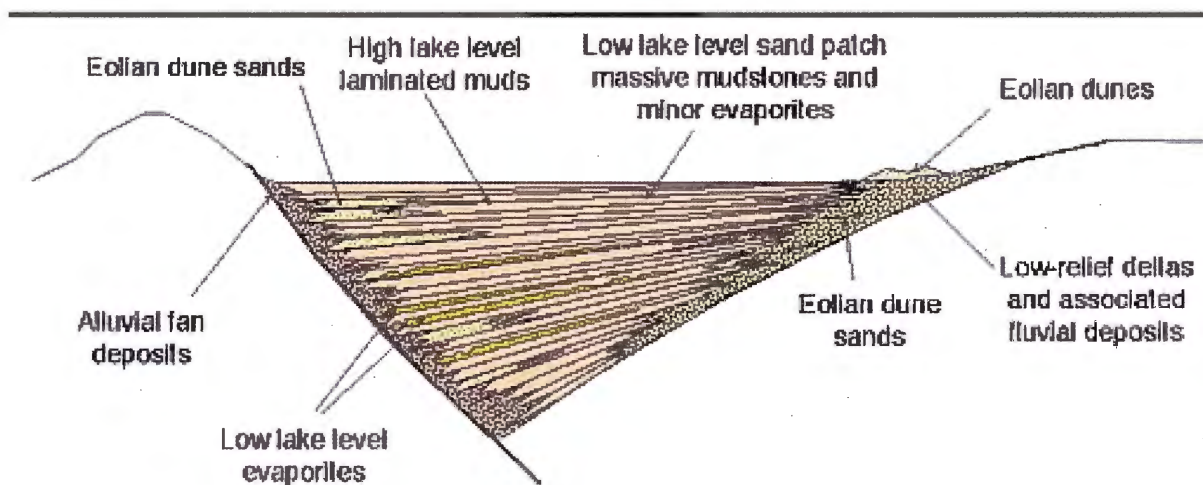


Figure 1.6: Fundy-type basin geometry analogue. The Triassic Wolfville formation likely developed in an environment like the one represented by the left hand side of this diagram, modified after Olsen, 1990.

1.5 Mesozoic Depositional Environments

The sediments of the Wolfville formation were likely the first preserved strata as rifting began to open the Fundy basin (Fig. 1.7). As high relief faults, escarpments and sloping basin margins began to develop, coarse-grained sediments began to be shed from surrounding areas of relief, depositing within conglomerates and alluvial fans. Aeolian dunes and caliche paleosols within the Wolfville provides evidence of a semi-arid to arid depositional environment (Hubert 1984). With basin fill and decreased accommodation space, coupled with a lower gradient along the basin margin, alluvial fans gave way to extensive braided channel deposits and deltas through the Mesozoic.

The Wolfville Formation has an estimated thickness of 700 m. The high degree of lateral variation exhibited by this unit in the form of cross-cutting and vertical stacking of large and small bar forms with fining upward successions and the lack of silts and muds is typical of a fluvial, conglomeratic braided channel environment. This study focuses on the strata of the lower 50 m of the Wolfville Formation.

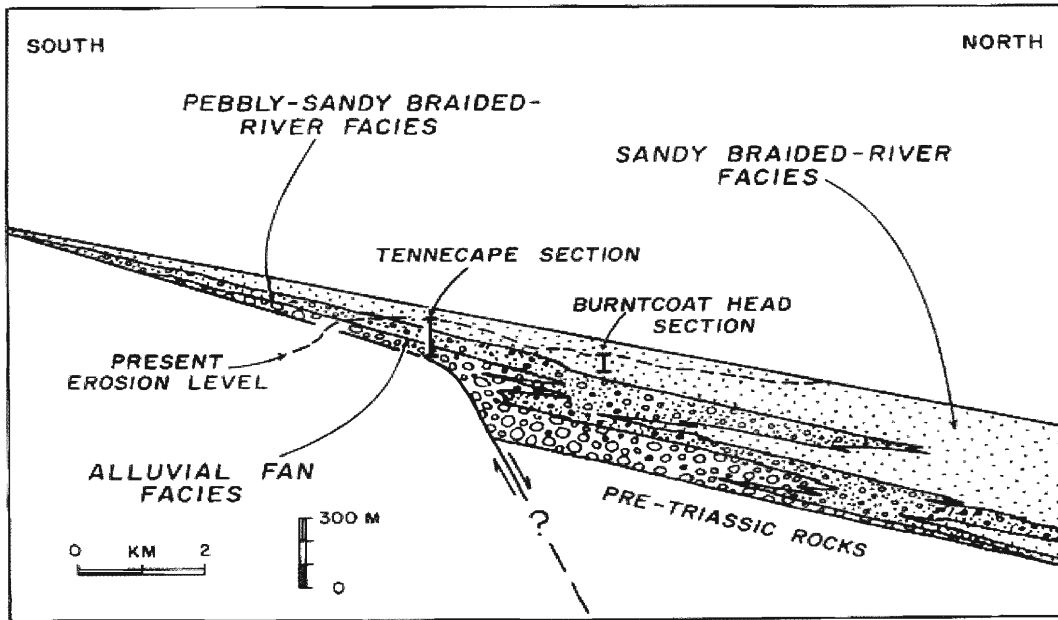


Figure 1.7: Depositional Model for the margins of the Minas Basin and the Wolfville formation in Nickerson, 2010, after Hubert and Florenza, 1988.

1.5.1 Alluvial fan deposits and facies

Alluvial fan deposits are typically characterized by loosely consolidated, poorly sorted sediment and commonly develop via traction currents down slope from regions of high relief, common along the margins of sedimentary basins. Alluvial fans (Fig. 1.8) are often activated by ephemeral or semi-permanent stream and river systems that can reorganize and rework the deposits. In arid environments, alluvial fans are often subjected to flash flooding events which can cause frequent avulsions that reorganize the fluvial systems operating on the surface of the fan.



Figure 1.8: A modern alluvial fan viewed from space. This fan has been repeatedly reworked by semi-permanent braided channel river systems. This is an excellent example of a modern analogue to the depositional environment in which the Wolfville formation sediments likely represent reworked alluvial sediments (Photo: NASA 2010). This photo is oriented to reflect the direction of flow and deposition at Cambridge Cove.

Poorly stratified, poorly sorted, matrix-supported conglomerates with lenses of clast supported breccia are common in this section. The matrix is very fine massive sand to silt with entrained angular clasts up to 10 cm in diameter. Many of the clasts were locally derived from underlying Carboniferous Horton group strata but other exotic, extra-basinal lithic clasts are

present. Their poorly sorted fabrics may suggest transport and deposition by debris flow or small-scale mass-wasting events. Lenses of clast-supported conglomerate likely reflect subsequent fluvial reworking of the debris flows. Locally clast-poor, matrix supported conglomerates with aligned clasts form sheet like beds with a medium to coarse-grained, sandy matrix. These clast-poor conglomerates may represent sheet flood events.

1.5.2 Braided channel deposits and facies

Braided channel and low sinuosity river systems (Fig. 1.9) have dominated fluvial style throughout geologic time. The development of vascular plants in the early Paleozoic resulted in bank stabilization and allowed for a wider range of styles during the Paleozoic (Davies and Gibling 2011). Nevertheless, these coarse bedload deposits remain prominent and persisted after the Devonian, reflecting the high sediment supply within orogenic systems.

Braided channel deposits occur as mobile channel belts laid down by low sinuosity channels. These deposits contain a diverse suite of sand-bed and gravel-bed rivers with braided and wandering channel platforms. The principal sedimentary features are bank-attached and in-channel bar forms and channel-base dunes (Gibling 2006). Fining-upward successions, local fines and abandonment fills and multi-story, stacked bar forms are common features with bar forms often showing divergent paleo-flow indications. In some cases, overbank fines and paleosols are well developed where lateral confinement is limited.

The common geomorphic settings for braided and low sinuosity rivers are unconfined plains, delta tops and large alluvial fans and the rivers can be either mountains-fed or plains-fed or a combination of both. They are dominated by vertical accretion where thicker bodies represent superimposed channel belts that swept across plains and amalgamated through avulsion

or were confined in fault-bound basins or broad valleys. These deposits can frequently reorganize in response to tectonism, avulsion, abrupt changes in lateral confinement or base-level change. The sometimes extreme vertical accretion in these deposits is often attributed to periods of active tectonism, rapid subsidence and enhanced coarse sediment influx. Many orogenic belts and volcanic islands have regularly spaced river exits, possibly tectonically controlled, which act as restricted points of access to a basin or the marine environments. This restricted access can result in the development of superimposed deposits or the coalescence of channel deposits from adjacent exits (Gibling 2006).



Figure 1.9: Aerial view of a modern analogue to the braided channel complexes of the Triassic Wolfville formation (Photo: USGS: Braided channel of the North Fork Toutle River, Washington).

Beds of clast-to-matrix supported, cross-stratified conglomerates constitute a considerable portion of the section studied at Cambridge Cove. The conglomerates are poorly sorted with clast sizes ranging from granules to cobbles (up to 30 cm). The matrix is medium to very coarse sand and the lithic-clasts are sub-angular to well-rounded. Trough and planar cross stratification is common and most bedforms show a fining upward character. These

conglomerates form the large, preserved barform deposits (Fig. 1.10) observable in the outcrop and in 3D exposures in the intertidal zone and are interpreted to represent bedload deposits of a braided river system which preserve channel fill and barforms (Fig. 1.11) (Leleu et al. 2009). These conglomerates are locally present within re-worked alluvial sediments. In parts of the section, these braided channel deposits directly overlie the unconformity and in some areas were deposited in topographic lows that cut into the underlying Carboniferous strata.

The barforms preserved in the intertidal zone at this location are typically 1m high, 5m long and 3-4m across. These formations likely became preserved following flood stage deposition, burial and subsequent lithification. Developing in a braided stream environment, these forms become elongate in the direction of paleo-flow. They typically form pseudo-diamond shapes as they are repeatedly avulsed and dissected by new streams and their geometries are re-organized.



Figure 1.10: 3D exposure of a preserved braided channel barform in the intertidal zone with Jordan Nickerson for scale. These barforms are excellent indicators of paleo-flow direction (red arrow)

The barforms displayed above are an excellent indicator of paleo-flow direction. These bar forms develop an elongate shape with the lee side approximating down-stream direction. The strike and dip along the top of these forms provides excellent indication of paleo-flow. The barforms observed in the Wolfville Formation all show evidence of having an approximate northerly paleo-flow direction.

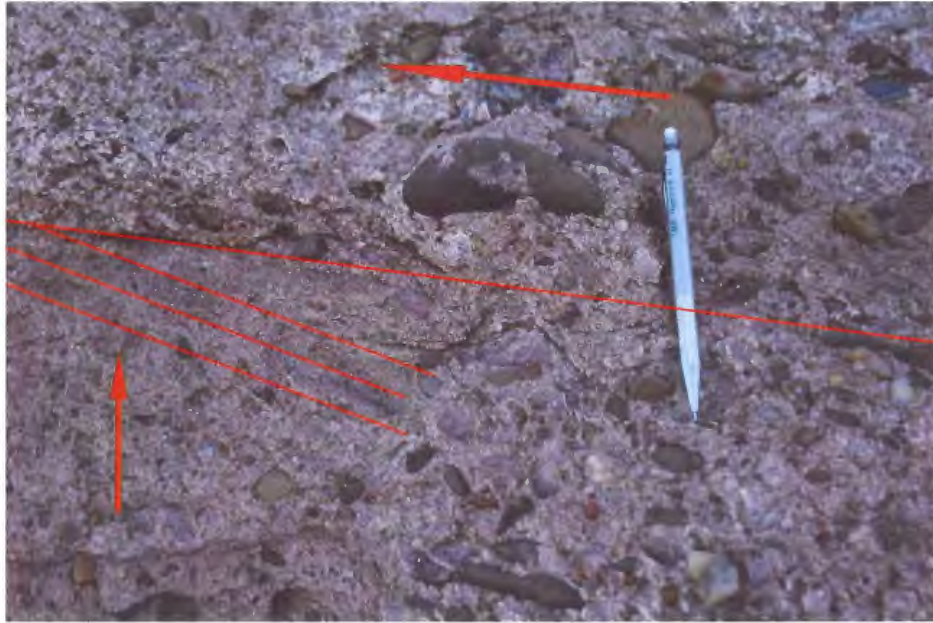


Figure 1.11: Bedload deposits of a braided river system which preserve channel fill and barforms. These conglomerates are locally present within relict alluvial sediments. Paleo-flow is indicated by clast imbrication (top arrow). Fining upward successions and cross strata are depositional indicators of barforms (bottom arrow).

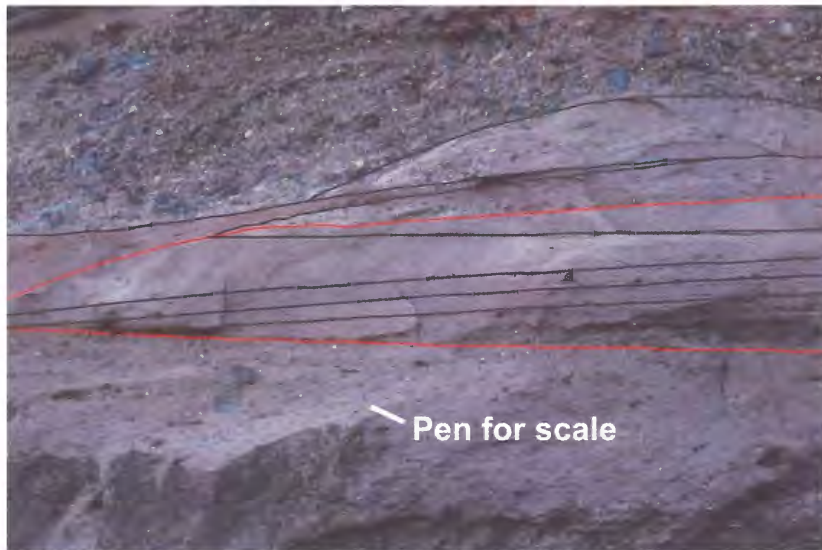


Figure 1.12: Coarse, lithic, pebbly sandstones. These sandstones are interpreted to represent bedload deposits of the braided river system, comprising channel fills and smaller scale dunes. These are also locally present in relict alluvial-fan sediments as stream flows and contain planar/cross beds.



Figure 1.13: Classic isolated block exposure at Cambridge Cove displaying complex internal geometries of the Wolfville braid channel complex.

Coarse, lithic, pebbly sandstones (Fig. 1.12) comprised of sub-angular to sub-rounded, medium-to-coarse grains with some pebbles and cobbles show trough and planar cross-stratification with some rooting. Paleosols with carbonate nodule horizons are occasionally developed on top of these units. These sandstones are interpreted to represent bedload deposits of the braided river system (Fig. 1.13), comprising channel fills and smaller scale dunes.

1.5.3 Structural elements and geometries

Fluvial channel bodies are three-dimensional forms generated by fluvial processes through time. These forms are single, interconnected mappable bodies of sand with a definite geometry and there are few terms available to describe them in 3D. Gibling (2006) notes two distinct sets of terminology for describing channel bodies in 2D and 3D. In cross sectional view (Fig. 1.14), channel bodies can be divided into single- and multi-storey bodies where there is commonly a central body and wings. Many bodies contain abundant erosional surfaces that could represent short term events such as floods. These bodies are termed *erosion-dominated*. The Wolfville Formation braided channel complex is classified as erosion-dominated.

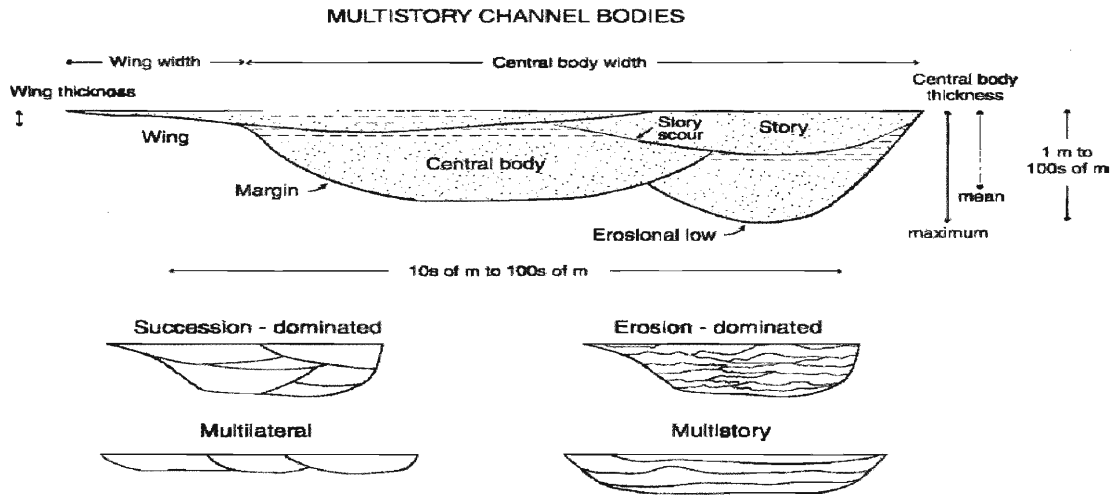


Figure 1.14: Terminology for describing the cross sectional geometry of multi-story channel bodies, after Gibling, 2006. The Wolfville Formation is classified here as Erosion – Dominated. In the Wolfville formation, large (up to 5 m) barforms are stacked as “stories” on top of or on the flanks of channel bodies.

3D classification of channel bodies will be based on the terminology outlined in Figure 1.15. Where possible, this classification scheme has been used to identify and classify any channel body features observable in subsurface GPR or outcrop LiDAR data. The diagram below is based on valley fills with distinct branches and tributaries, but the terms may also be applicable to broad channel bodies with a complex history and internal geometry.

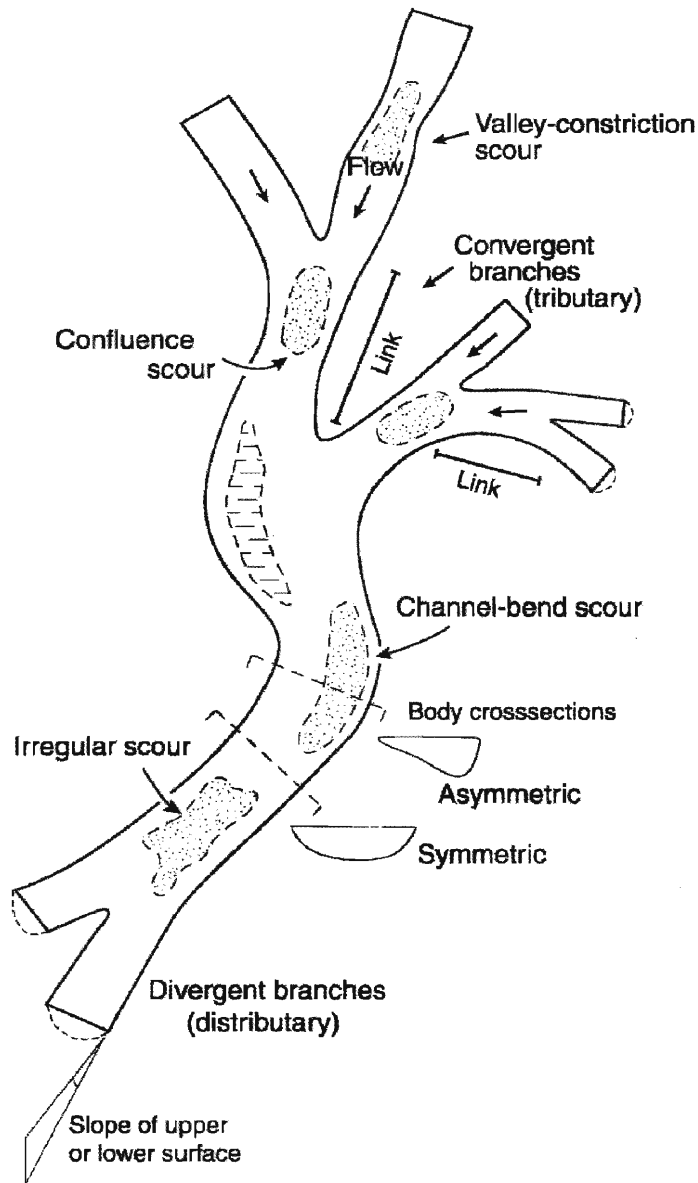


Figure 1.15: Terminology for describing the three dimensional form of channel bodies after Gibling, 2006.

Throughout the extensive 300m section of the outcrop at Cambridge Cove (Wolfville and Horton Formations), several normal faults were observed and in at least two cases form flower structures or small horst-graben pairs (Fig. 1.16). In this area, fault orientations were observed and recorded during field work.

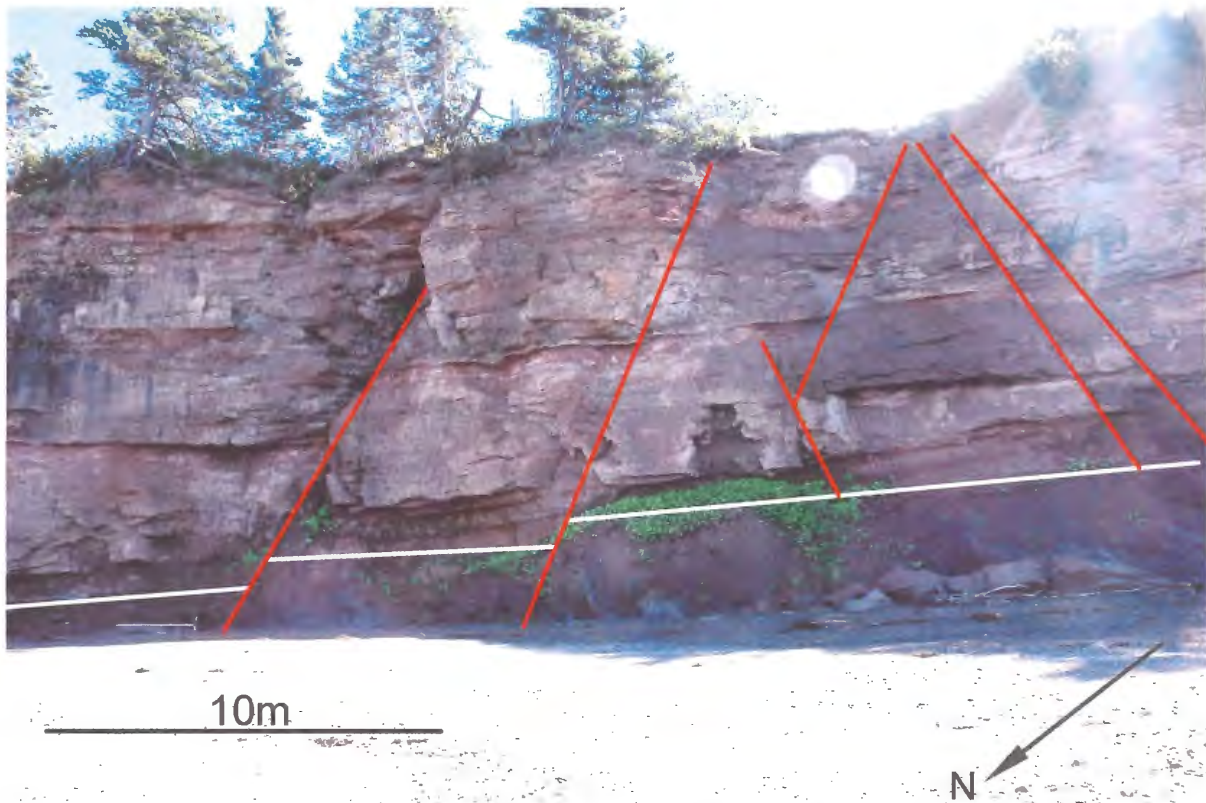


Figure 1.16: Normal faults and flower structure visible in 15-20 metre high cliff section at Cambridge Cove. Much of the displacement along these faults may be along-strike due to dextral transpressional movement along the Minas Fault Zone.

The faults seen here along the shores of the Fundy Basin truncate both the Carboniferous and Triassic formations in some cases, based on the dislocation of the unconformity surface.

These north to northwest striking normal faults likely developed through dextral transpression due to strike-slip motion along the Minas Fault Zone (Waldron et. al, 2007). Throws along these faults are typically no greater than 2 metres locally as seen by the apparent displacement of major stratigraphic units across the faults. Lateral motion along the fault planes could not be accurately discerned. Where possible, the orientation of these fault planes will be used to estimate where these structures should appear in the subsurface data set behind the outcrop.

The section of outcrop of particular interest at Cambridge Cove was previously described and correlated in a series of measured sections in 2009 (Nickerson 2010). The measured sections were acquired by rappelling down from the top of the cliffs and completing detailed stratigraphic

logs (Fig. 1.17). Measured section 5 was recorded at a section of outcrop immediately adjacent to the GPR survey region and provides more stratigraphic control for correlation from GPR to outcrop.

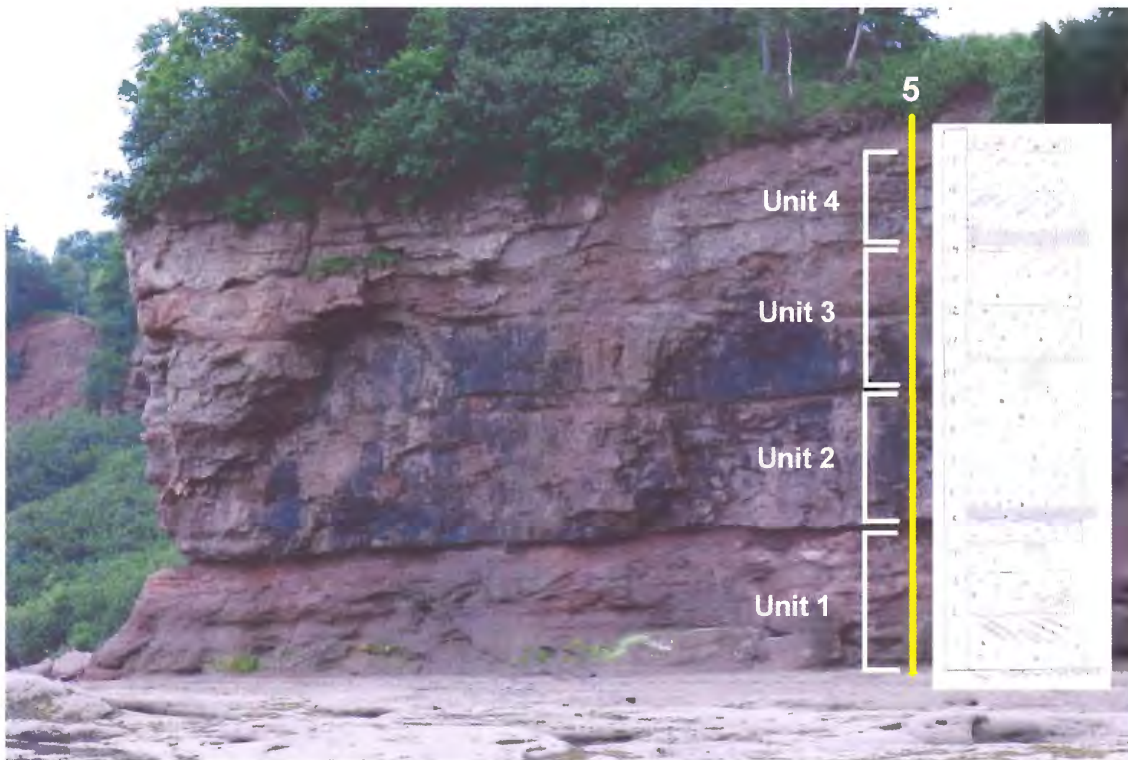
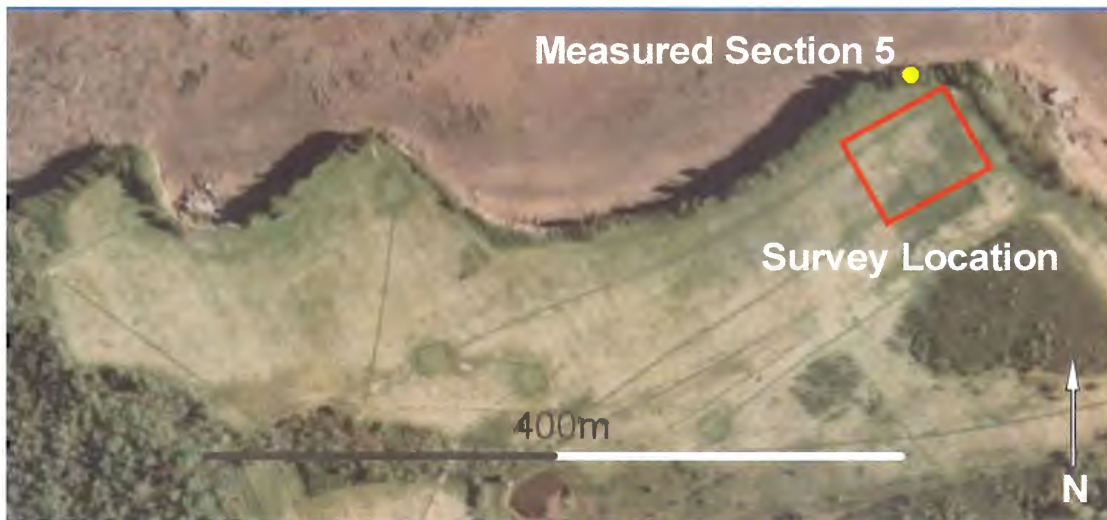


Figure 1.17: Top: Location of measured section 5 relative to the GPR survey location. Bottom: Outcrop view of measured section 5 after Nickerson, 2010.

CHAPTER 2: METHODOLOGY

2.1 Introduction:

Geophysical methods such as shallow reflection seismic profiling and GPR present continuous subsurface profiling methods which can provide high-resolution Reconstructions of depositional environments (Jol and Smith 1991).

Ground-penetrating radar (GPR) is a non-invasive geophysical technique that detects electrical discontinuities in the shallow subsurface. The GPR transmits discrete pulses of high frequency electro-magnetic (EM) energy, generating a wave-front that propagates downward into the subsurface. Some of the energy is reflected back to the surface because of a change in the bulk electrical properties of different subsurface lithologies (e.g., sand and mud). At the surface a receiver monitors reflected energy versus delay time. This delay time is a function of the EM velocity of propagation through the sediment and the depth of subsurface reflectors. GPR provides a profile of horizontal survey distance in metres versus two-way vertical travel time in nanoseconds. By estimating the propagation velocity in the sediment, the depth of reflectors can be determined (Jol and Smith 1991).

Since the mid 1990's, sedimentary geologists have used various GPR techniques to conduct sedimentological studies in order to reconstruct past depositional environments and to explore sedimentary processes in a number of environmental settings. These methods have been used to aid in hydro-geological investigations and have been instrumental in various hydrocarbon reservoir analogue studies. In processed radar profiles, primary reflectors usually indicate primary depositional structures, as they represent lithological and therefore electrical discontinuities (Neal 2004).

The increased use of GPR data acquisition methods for shallow subsurface investigations is due to the recognition that sub-metre vertical resolutions are possible and not obtainable with typical seismic reflection and refraction methods. EM waves have greater depths of penetration through ice and snow compared to non-frozen substrates and therefore the technique was originally applied to glaciology as early as the 1920's (Plewes and Hubbard 2001). However, it was not until the 1980s that GPR became commercially available and its application in engineering, archaeology, forensics and geology became more common.

Despite the wide use of GPR, there are a number of fundamental problems that remain in its application to sedimentological research. There are wide ranging, highly variable approaches to the processing, interpretation and acquisition methodology for GPR data with little consensus on common methodologies. In order to acquire meaningful sedimentological data using GPR, it is essential that one has a thorough understanding of the limitations and implications of each step required in the acquisition, processing and interpretation of the data. The underlying scientific principles explored in this section formed the primary controls on methodology design for this study. These principles include: considerations of the data acquisition regime, the finite resolution, depth of penetration, the cause of reflectors not related to primary sedimentary structure and the practical application of data processing techniques that fit the overall aim of the study.

The methodologies employed for this study, the theoretical causes of subsurface GPR reflections, the inherent limitations of unprocessed GPR data and the data processing techniques applied to the acquired data will be examined in the following sections.

2.2 Data Acquisition

Data acquisition in the field was conducted over four day trips to the Minas View golf course, in April, September and October of 2010 and January of 2011. The course is situated immediately above and behind the outcropping of Triassic Wolfville Formation strata at Cambridge Cove, along the shore of the Minas Basin, Nova Scotia. Survey equipment and personnel were transported by motor vehicle to the field location and moved across the course using a golf cart. In the case of the January field trip, the cart was pushed to the survey location. Three locations were selected over which to conduct subsurface surveys (Figure 2.1). These sites were located based on what subsurface features were being targeted, and the acquisition methods were tailored based on the geometric scale of these features. Since depth of penetration and resolution are frequency dependent (with wavelength governing resolution and overall frequency governing penetration), larger scale geometric features such as regional faults and the major Mesozoic-Paleozoic unconformity were targeted using lower frequency, 50 MHz antennas, while braided channel bar forms and channel margins were targeted using 100 and 200 MHz antennas.

In order to develop a 3D framework in which to examine and resolve these subsurface features, the survey lines were organized into X-Y grids with equally spaced lines. If spacing in these lines is close enough, the parallel traces will contain some of the same reflection data and volumetric cubes of data can be generated. These grids were geometrically defined by measuring tape, lawn spikes and measured ropes. The lines were walked based on lines of sight and with laid down ropes. On-board GPS equipment was used to record line transects of these grids for future georeferencing.

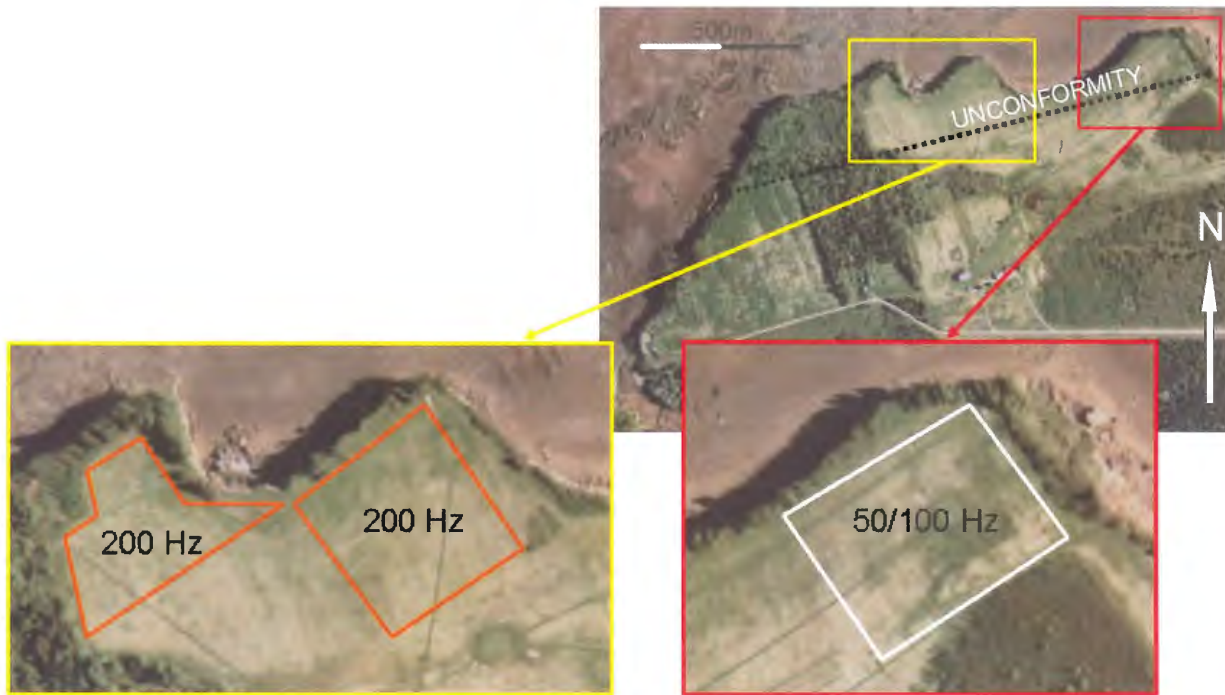


Figure 2.1: Aerial view of study areas where GPR data was acquired as X-Y grids and the respective frequencies used at each location.

2.2.1 Differential GPS

One essential element in generating a high resolution, spatially correct GPR grid survey, is to have both precise and accurate location data to georeference acquired data in 3D space. Standard GPS systems have a built-in error (because higher-accuracy GPS signals are proprietary to the US government and are not publically available on basic, non-differential systems) on the order of several metres in the horizontal X and Y planes and in some cases over 10m of error in vertical accuracy. This lack of vertical accuracy in particular causes problems when correcting a subsurface profile for variations in surface topography in the area where the data were collected. Since the GPR cart is constantly moving and shaking while the survey progresses, GPS fixes are often degraded or lost during the process of the survey, resulting in anomalous topographic readings that will shift large portions of a subsurface profile along the x, y or z axes. These errors

could potentially produce subsurface artefacts that could subsequently be misinterpreted as real features.

The first three surveys conducted for this project (both 200 MHz surveys and the 100 MHz survey) were conducted using the standard GPR equipment built into the GPR cart and did not employ the use of Differential GPS (DGPS). As a result, these surveys contain good subsurface data, but poor quality GPS positions. Therefore, the only data set used in this current work will be the 50 Hz survey conducted on the eastern extent of the golf course, which was conducted using DGPS. It is recommended that a properly geo-referenced GPR line be acquired between all these data sets to properly ground truth them for integration into a larger scale survey.

In order to minimize and eliminate these GPS errors, a differential GPS system was integrated into the data acquisition process and coupled with the GPR equipment. In this survey, a Leica GPS1200+ Series High Performance GNSS system (Fig. 2.2) was used to obtain real-time GPS positions accurate to less than 2cm in all directions. Differential GPS is an enhanced system that is based on a fixed base station that broadcasts the difference between its position indicated by the satellite systems and its accurately surveyed position. A DGPS base station will track and record the “wander” in the position of a stationary point as indicated by orbiting satellites. A roving receiver attached to the GPR cart acquires its own GPS position and is in communication with the base station via UHF radio transmitters. As the rover obtains GPS coordinates, the wander as recorded by the base station is subtracted in real time from these coordinates and these corrected points are recorded into the GPR profile dataset via the GPR cart computer. The result is an extremely accurate GPS data set that provides highly accurate topographic corrections and grid survey line positioning.

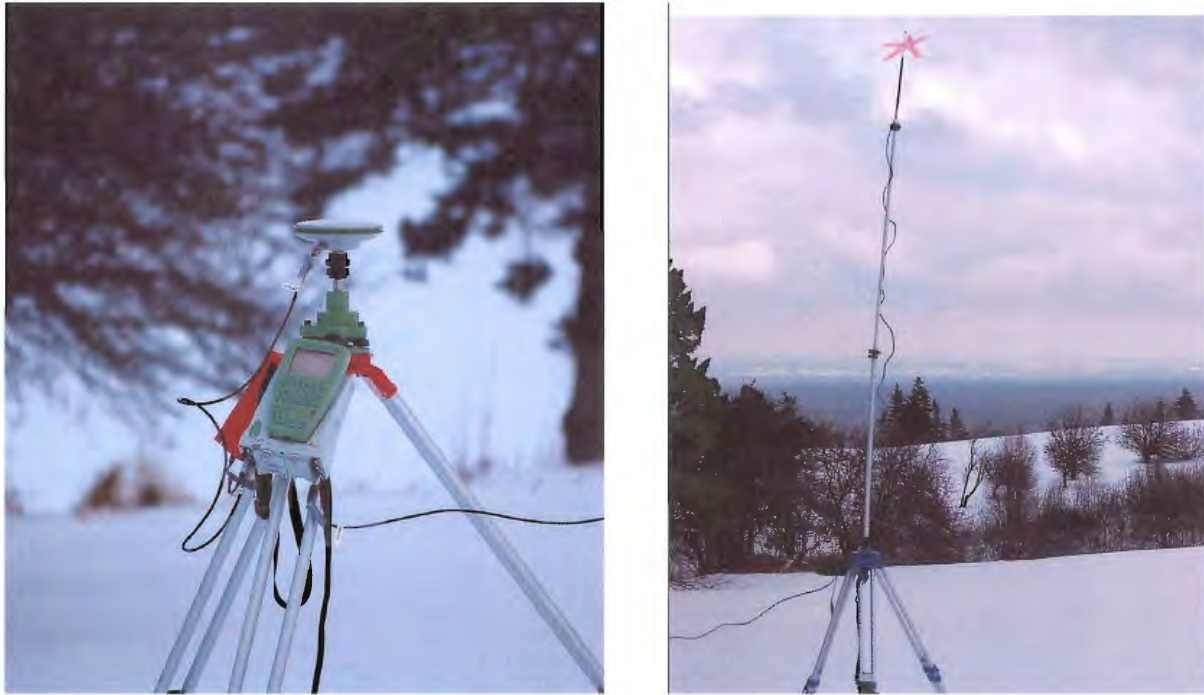


Figure 2.2: Left: Leica 1200 DGPS base station. Right: Radio transmitter and antenna.

2.2.2 Ground Penetrating Radar

This study employs the use of reflection profiling using common offset geometry. Common offset surveys are used frequently in GPR studies and in this case, the equipment (Fig. 2.3) consists of separate transmitting and receiving antennas at a fixed-spacing, both oriented in the same direction and held perpendicular to the survey lines. With such an antenna configuration, the survey geometry is said to be co-polarized, perpendicular broadside (Fig. 2.4). To conduct the survey, the antennae are dragged along the ground and horizontal distances are measured with an on-board odometer which functions as a trigger timer. In this particular study, the fourth attempt at data acquisition was conducted in January 2011 and the survey location was under considerable snow cover. These weather conditions called for a modification to the GPR equipment such that it could operate and acquire data in snow. The wheels of the cart were fitted

with customized downhill skis and fixed so that they could not rotate and the cart would glide near the top of the snow cover.

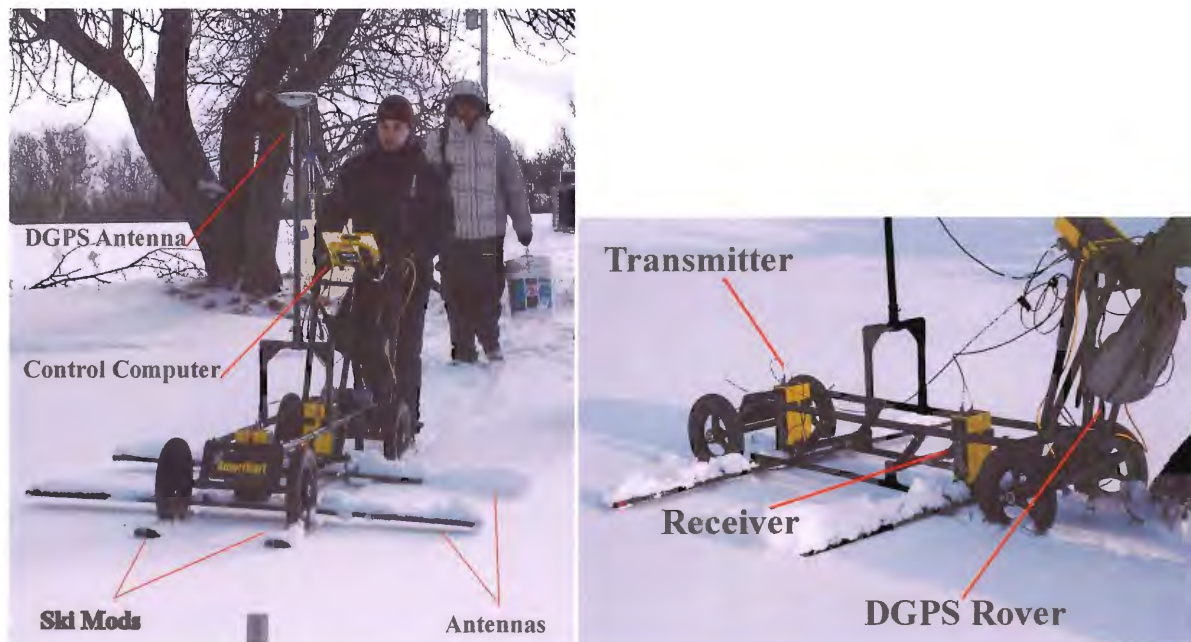


Figure 2.3: GPR Cart anatomy.

This configuration does not allow for the use of an odometer as a shot timer or measure of distance. Therefore, the equipment was set to acquire data continuously with a shot spacing calculated from DGPS position fixes during post processing. In comparison to this cart configuration, in several other surveys the equipment is moved in a stepwise manner at fixed horizontal intervals and antennae are held stationary during data acquisition. The later method generates more coherent, higher amplitude reflections because of better ground-antenna coupling, but it takes much longer to complete a survey grid. In this instance, the snow cover served to improve the coupling of the antennas with the surface and provided a much smoother ride compared to surveys conducted over solid ground.

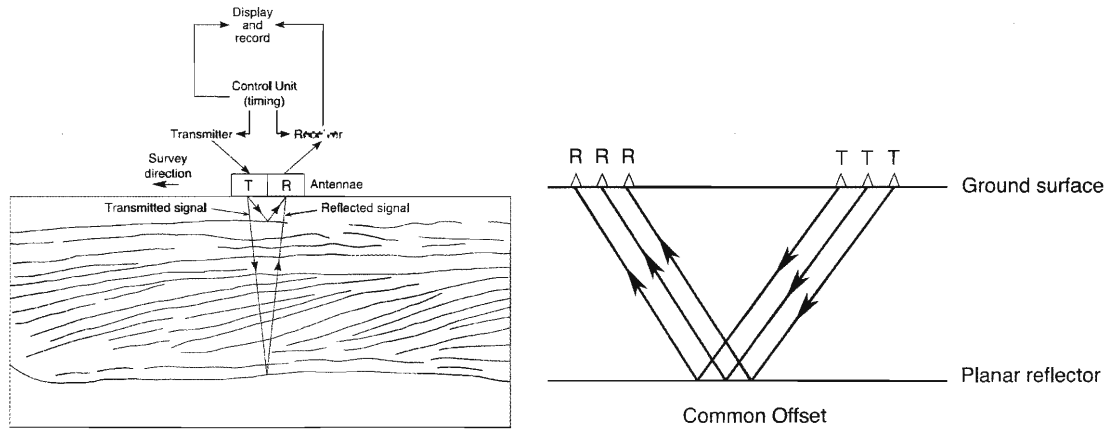


Figure 2.4: Left: Data acquisition at an individual survey point, showing GPR components and hypothetical subsurface reflections. Right: Common offset survey geometry. T= transmitter, R= receiver after Daniels, 1996.

As the equipment is pushed and data are recorded during the survey, sequential reflection traces are gathered and stacked side by side to build up a radar reflection profile. Each trace results from the system emitting a very short pulse of high frequency electromagnetic energy that is transmitted into the subsurface. As the pulse propagates and encounters materials of differing electrical properties, its velocity is altered. If these changes are abrupt with respect to the dominant wavelength of the pulse, some of the pulse energy is reflected back to the surface. The reflected signal is detected by the receiving antenna. The time between transmission and detection, referred to as the two-way-travel time or TWT, is measured in nano-seconds, much faster than the typical milliseconds or seconds used with reflection seismology, and is a function of depth, the antenna spacing, and the average radar wave velocity in the overlying material.

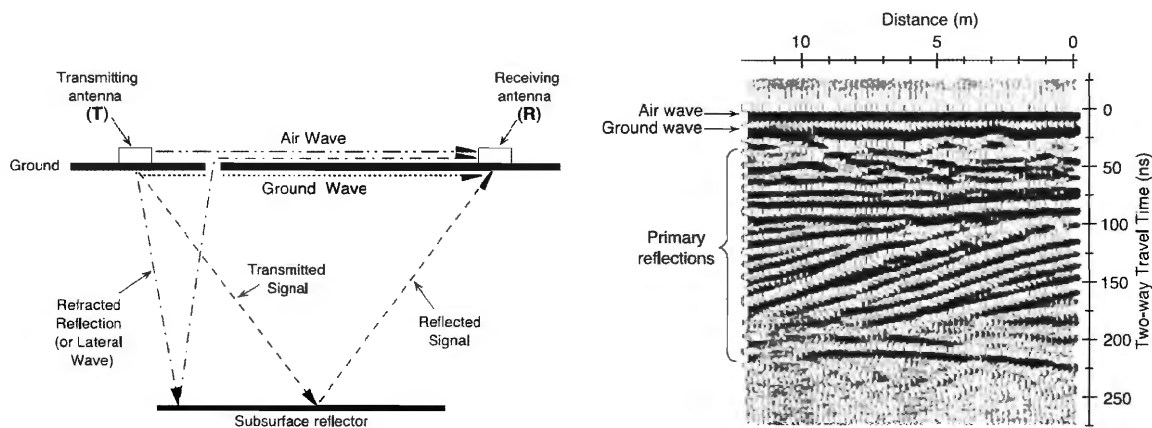


Figure 2.5: Left: Ray paths between transmitting and receiving antennae for the air wave, the ground wave, the refracted wave and a reflected wave after Daniels, 1996. Right: Radar reflection profile resulting from sequential plotting of individual traces from adjacent survey points after Neal and Roberts, 2000.

There are a number of signals generated and received by the equipment that do not represent subsurface reflections and must be accounted for in data processing considerations. The first pulse to arrive at the receiving antenna is the air wave (Fig. 2.5) which travels between the two antennae at the speed of light. The second arrival is the ground wave which travels directly along the ground-air interface from the transmitting to the receiving antenna. These arrivals can mask any primary reflectors in the uppermost part of the reflection profile. Last to be detected are the reflected arrivals, which are of primary interest.

GPR Reflection Theoretical Background

There are three primary controls on the behaviour of electromagnetic energy in a medium (Neal 2004). These are dielectric permeability (ϵ), electrical conductivity (σ) and magnetic permeability (μ). The velocity (V) of an electromagnetic wave is a function of its frequency, the speed of light in free space, and the host medium's characteristics as defined by the above variables. This is mathematically defined by the following expression:

$$v = \frac{c_0}{\sqrt{\epsilon_r \mu_r \frac{1 + \sqrt{1 + (\sigma/\omega\epsilon)^2}}{2}}} \quad (2.1)$$

-where c_0 is the electromagnetic wave velocity in a vacuum, and $\sigma/\omega\epsilon$ is a loss factor, where $\omega=2\pi f$ is the angular frequency. This expression can be simplified for low-loss materials (limited attenuation of signal during propagation compared to less homogeneous materials) like clean sand and gravel where the influence of both electrical conductivity and magnetic permeability are assumed to be negligible (Reynolds 1997). As a result, the above equation simplifies to:

$$v = \frac{c_0}{\sqrt{\epsilon_r}} \quad (2.2)$$

As the electromagnetic wave propagates through the medium, its amplitude (A) attenuates exponentially from its initial value (A_0) as it travels distance, z as follows:

$$A = A_0 e^{-\alpha z} \quad (2.3)$$

Where α is the attenuation constant. For low-loss materials, this constant is frequency independent, such that:

$$\alpha = \frac{\sigma}{2} \sqrt{\mu/\epsilon} \quad (2.4)$$

Based on the assumptions that are used to derive these equations, a number of assumptions about the behaviour of electromagnetic fields in earth materials can be made. Since water exhibits a high value of ϵ compared to air and typical rock-forming minerals, water saturation will exert the primary control over the dielectric properties of common sedimentary materials. This has significant implications when considering the regime in which a survey is

staged, since water-saturated sediments will yield bright water table reflections on the profiles. However, the assumptions above break down when highly conductive substances such as sea water or significant amounts of magnetic material such as magnetite or hematite-rich clays are present. Since the primary dataset of interest for this study was obtained in January above a substrate likely frozen within 1 to 2 metres of the surface, the problem of ground water saturation may have been reduced.

When propagating magnetic fields encounter a significant subsurface electrical discontinuity, some of the incident energy is reflected. The amount of energy reflected is defined by the reflection coefficient (R). Assuming that electrical conductivity and magnetic permeability contrasts are negligible:

$$R = \frac{\sqrt{v_2} - \sqrt{v_1}}{\sqrt{v_2} + \sqrt{v_1}} \quad (5)$$

where V_1 and V_2 are the velocities of adjacent layers 1 and 2. In all cases, the value of R lies between +1 and -1. Reflection coefficient modelling for subsurface discontinuities in various unconsolidated sediments suggest that radar is sensitive to changes in the sediment/air/freshwater ratio (Baker 1991).

Limitations of Unprocessed Data: Key Issues

There are a number of inherent limitations, errors and noises associated with raw, unprocessed GPR data, many of which are comparable to those associated with raw seismic data. These limitations and noises need to be considered and corrected for in order to extract meaningful sedimentological information from the data.

Normal moveout

Although common off-set data collection is popular as a convenient and quick method for obtaining radar reflection profiles, there is an inherent limitation to this mode of data acquisition. Using non-coincident antennae causes image distortion due to an increase in TWT, depending on the distance between antennas. This error is commonly referred to as a normal moveout (NMO). The effect of normal moveout becomes less significant with increasing travel time and decreasing source receiver offset. In the case of this study, since the antennae offset is significantly less than reflector depths and the structural dips of the sedimentary horizons are shallow, hyperbolic normal moveout is a reasonable approximation of moveout and can be used to correct for the separation distance.

Depth of penetration

Propagating electromagnetic waves undergo significant energy losses as they move through the subsurface. This limits the depth to which radar waves at a particular frequency or location can penetrate. The magnitude of this attenuation is frequency dependent and in general, the higher the antenna's frequency, the shallower the depth of penetration. As energy levels attenuate, the amplitude of reflected waves decreases to the point where detection levels are too low or the signals are no longer visually distinguishable on a radar section, rendering deeper arrivals non-resolvable.

Vertical and horizontal resolution

Vertical resolution (Fig. 2.6) is a function of wavelet sharpness and pulse width and is directly proportional to frequency. As frequency increases, so does vertical resolution. This is controlled by wavelength (λ) and is governed by wave frequency and velocity such that:

$$\lambda=v/f \tag{6}$$

The most common frequency detected by the receiving antenna is typically lower than the centre-frequency emitted by the transmitting antenna. This is due to preferential attenuation of higher frequency energy during propagation and the diverse frequency content of the transmitted pulse. Therefore, it is more accurate to determine vertical resolution based on the return pulse. Wave theory suggests that the maximum obtainable vertical resolution is $\lambda/4$ (Nyquist principles). It follows that any layers that are thinner than $1/4$ of the wavelength of the incident pulse will not be properly detected (Fig. 2.7).

In GPR, the antennae function as dipoles that generate polarised fields. The shape of a propagating radar wave front is extremely complex and is complicated by the way in which the field convolves with the subsurface. This convolution leads to the development of a radar “footprint” (Fig. 2.8) that is elliptical in shape and is even further complicated when surveying over dipping reflectors. This causes a sharp decrease in horizontal resolution with depth and decreases the effectiveness of depth migration in post processing.

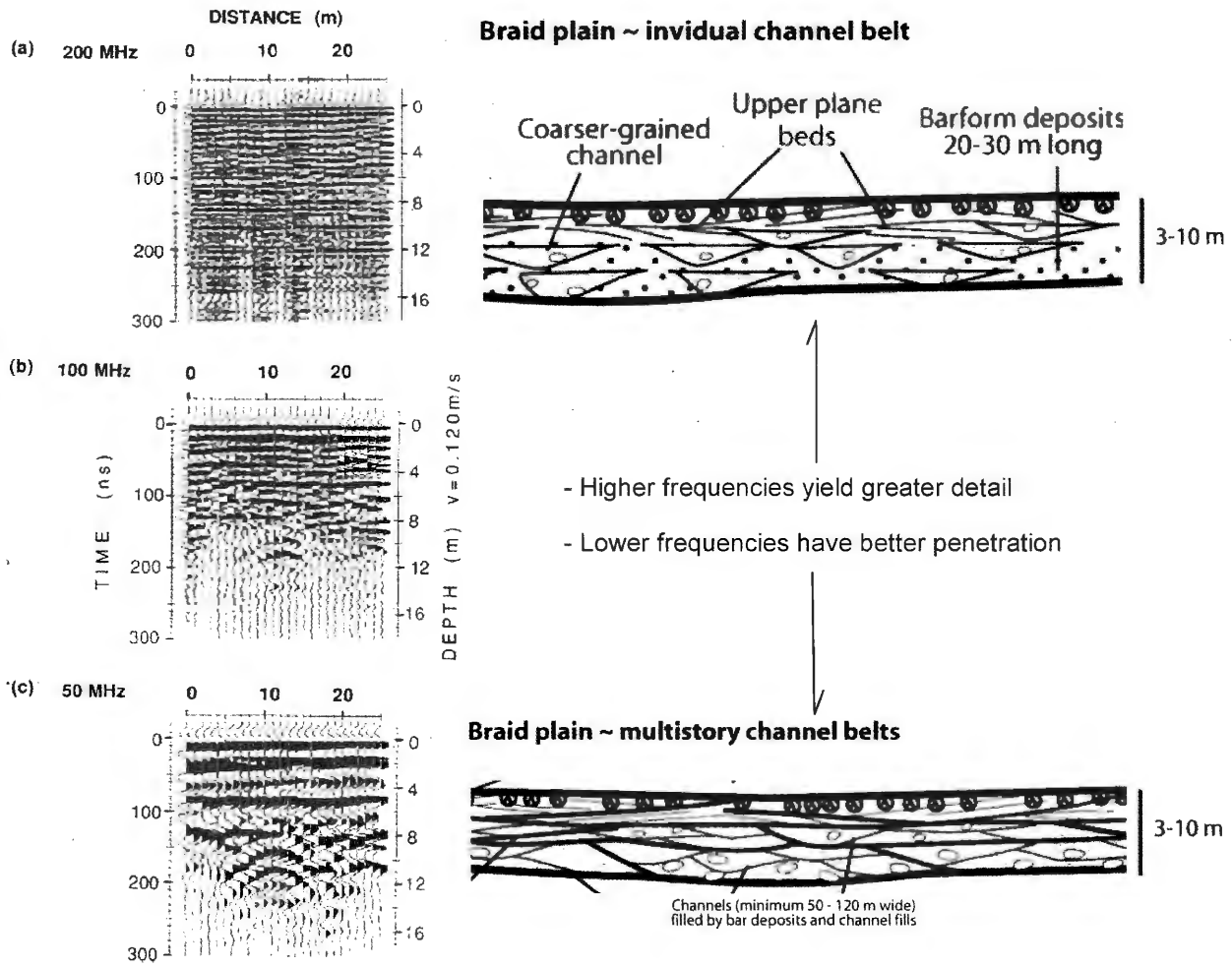


Figure 2.6: Left: Examples of GPR profiles acquired over the same section of subsurface with different frequencies (after Jol and Smith 1991). Right: A higher frequency signal will produce higher resolution data and can be used to image smaller-scale subsurface features such as bar forms and individual channel fills within single-story channel belts. Lower frequencies will have an increased depth of penetration but are more appropriate for imaging larger scale features such as channels and multi-story channel belts (after Leleu et al. 2009).

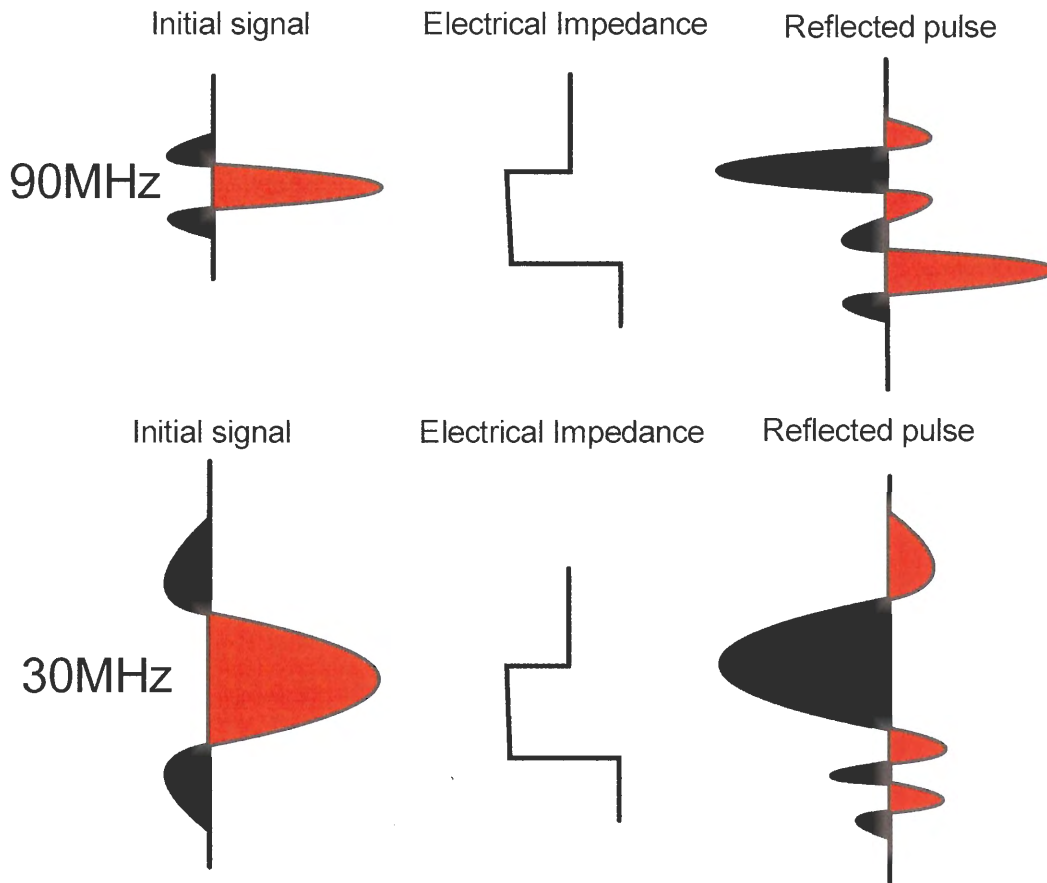


Figure 2.7: Comparison of reflections generated by sources of different frequencies. Resolution in the subsurface is a function of wavelength and therefore frequency. Higher frequency sources like the 90Hz source above provides better resolution than the 30Hz source, but the lower have better depth of penetration. Higher frequency energy attenuates more quickly in the subsurface.

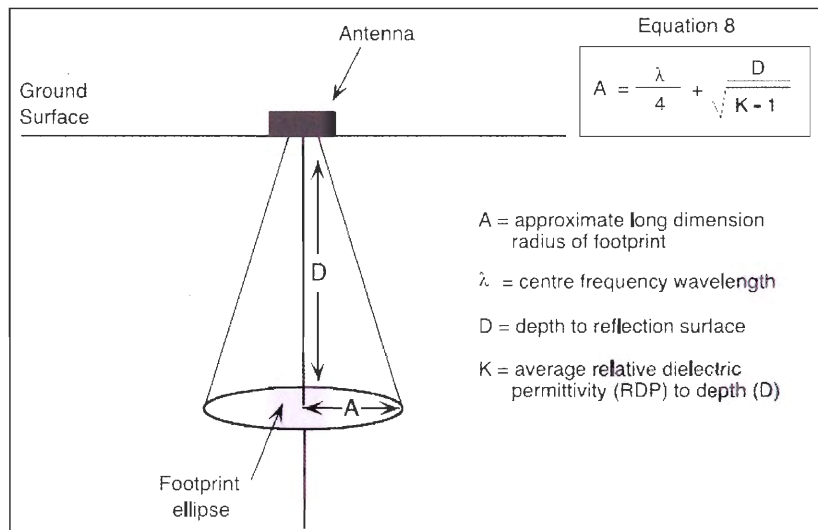


Figure 2.8: Radar elliptical footprint approximation after Neal 2004.

Diffractions, distortions, dip displacements

Since radar antennae radiate and receive electromagnetic energy in a complex 3D cone, reflections recorded on the profile do not necessarily come from immediately below the survey point. Reflected energy can radiate from anywhere on the wave radar front and from various points on undulating subsurface reflectors. This can lead to errors in apparent dips, bowtie anomalies (Fig. 2.10) and diffractions from point anomalies that obscure primary reflectors (Fig. 2.9).

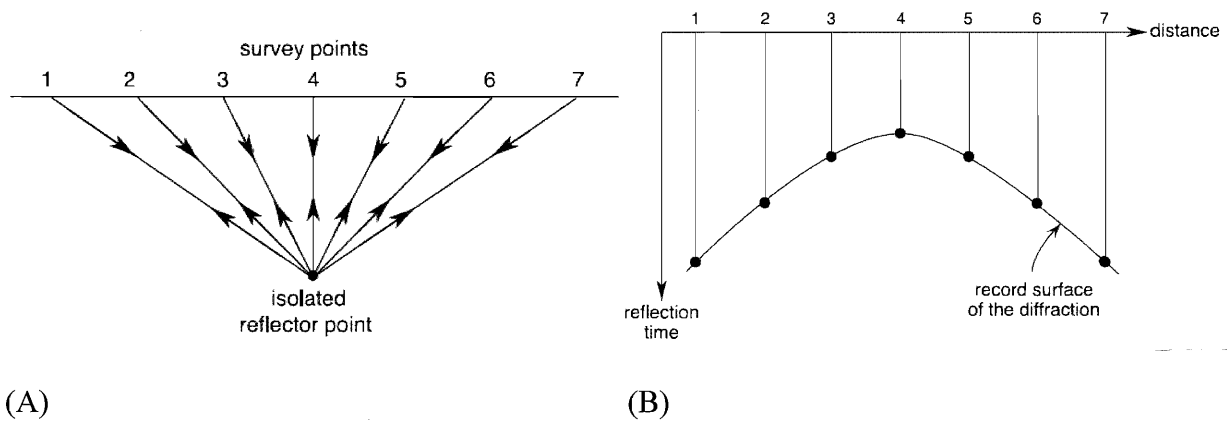


Figure 2.9: (A) Resolving isolated point reflectors. (B) Diffraction noise generated by isolated point reflector.

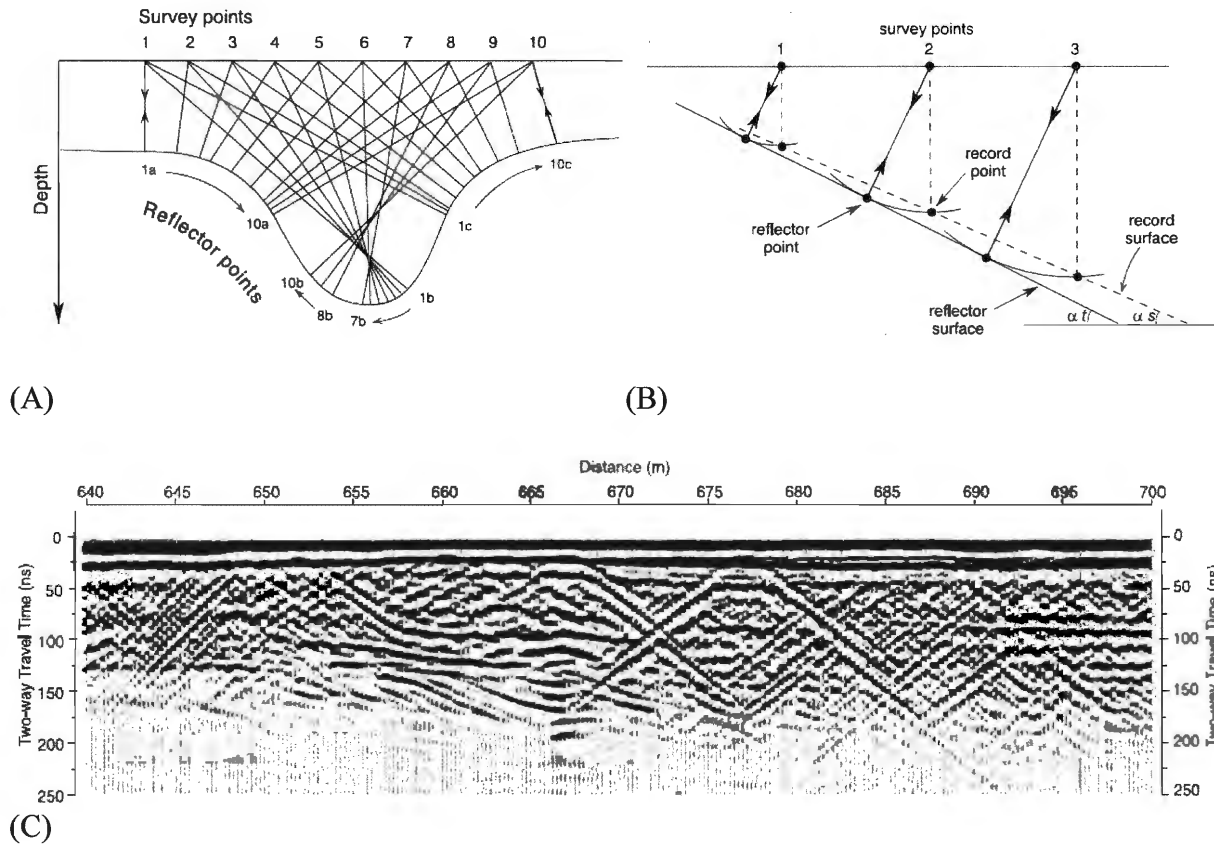


Figure 2.10: (A) Undulating reflector that can generate bowtie anomalies. (B) Errors in apparent dip. (C) GPR profile showing diffractions and apparent dips after Neal 2004.

Topographic variation along the survey line

Elevation changes along a survey line are not taken into account on raw radar sections.

This can lead to significant distortions of the subsurface images if not corrected for. This problem is made worse because the radiated energy from the transmitter is no longer directed vertically downward on slopes, but instead has a horizontal component that increases with increasing slope. At slopes greater than about 6 degrees, the subsurface reflections will be mislocated. Topographic variations are corrected using DGPS z-coordinates.

Ambient and systematic electromagnetic noise

Since GPR systems are essentially broadband receivers, they are highly susceptible to interference from various external, man-made sources of EM radiation. Examples include television transmitters, FM radio transmitters, mobile cell phones and towers, walkie-talkies, etc. These sources of EM noise are sometimes possible to avoid. Systematic noise can be generated within radar profiles in the form of “ringing multiples” or reflection events of various origins that obscure primary reflectors. Ringing is common where wire cables are used to connect the transmitter and receiver to the console. The effect of this type of noise is effectively reduced in this survey by employing the use of fibre optic cables instead. Ringing can also be caused when a signal bounces back and forth between a highly conductive reflector and the receiver a number of times (Sensors and Software, 2006). This can sometimes indicate the presence of highly conductive saline ground water and limits the use of GPR where saline waters are present.

Surface and Subsurface reflections

Although GPR antennae direct most of their energy into the ground, some energy is also dissipated into the air. When airborne radar waves strike an object or planar surface with high electrical contrast, the resultant reflected signal is recognized by the receiver. Therefore, on some radar profiles, not all reflections are of a subsurface origin. This is a common issue with unshielded antennae, but shielding limits the size of antenna and therefore the frequency. Common examples of surface reflectors are power lines and poles, trees, metallic fences, large boulders, walls and highly irregular topography. These surface reflections can sometimes be confused with, or obscure subsurface reflections. Common subsurface obstructions such as pipelines, metallic fence lines, irrigation systems, culverts and electrical cables can produce erroneous

reflections from the subsurface. Fortunately, none of these obstacles are known to exist beneath the survey area.

2.3 Data Processing

Data processing is an essential component to conducting any type of geophysical research. Raw subsurface data, as described above, contain several types of noise that need to be removed in order to yield useful subsurface profiles. The following section outlines the processes applied to the raw data during processing.

The processing software EKKO_View Delux, a software package designed by the manufacturer of the GPR equipment, Sensors and Software Inc., was used to inspect and process the raw GPR data. The data are first imported and sorted into X and Y grid lines and then DGPS fixes are associated with each line from a separate .gps file. In this instance, since an odometer was not used to compute shot spacing for this survey, the step size of the data was computed based on the DGPS fixes for each trace, resulting in an accurate line length. The survey was conducted in a reversing pattern so that adjacent lines start at opposite ends of the grid area. To account for this, the position data from every second line are reversed (Fig. 2.11). Once these procedures are complete, data processing methods are applied.

File Name	Start ...	Stop ...	Stepsize	Units	Time Window (ns)	Min Elevation	Max Elevation	GPS ...
XLINE00	0.0	359.0	0.5	m	400.0	0.0	0.0	No
XLINE01	0.0	335.5	0.5	m	400.0	0.0	0.0	No
XLINE02	0.0	331.0	0.5	m	400.0	0.0	0.0	No
XLINE03	58.478	0.0	-0.108	m	422.4	15.071	16.219	Yes
XLINE04	0.0	60.113	0.087	m	427.2	14.75	16.175	Yes
XLINE05	59.91	0.0	-0.11	m	428.8	14.726	16.15	Yes

Figure 2.11: XLINE00 – 02 are raw. XLINE03-05 have computed step size, topographic correction, DGPS fixes and line orientation corrections applied.

The relevant data processing techniques are applied within a processing window (Fig. 2.13). Various operations are added and applied in series with a number of different setting

considerations. The settings for each individual operation are determined following inspection of the content of the data. Amplitude vs. Frequency plots and Amplitude vs. Time plots (Fig. 2.12) are inspected for each line. These plots help to determine what settings are best when applying various gains and filters to the data.

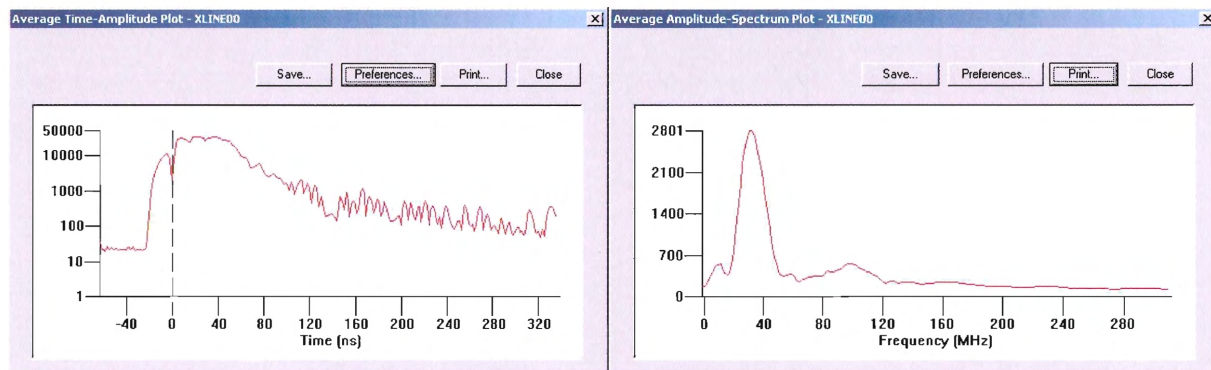


Figure 2.12: Left: Amplitude vs. Time of raw XLINE00. Right: Amplitude vs. Frequency of raw XLINE00.

Since the strata being surveyed here are unique to this project, the workflow developed by Jol and Smith (1991) has been modified employed for data processing. The resulting workflow is shown below in Figure 2.14. The first process selected in the workflow, the DEWOW filter, is designed to remove a slowly decaying low frequency “WOW” on each trace which is super-imposed on the higher frequency reflections. This process removes the unwanted low-frequency signal content while preserving the high-frequency signal.

The second process in the workflow is a DC shift that removes a direct current level from all the traces in the dataset. Its primary function is to reduce electromagnetic noise on the trace.

The third process in the workflow is a Bandpass filter. This filter is used to filter outside a certain bandwidth. It uses a Fast Fourier Transform algorithm to convert the data from the time – space domain to the frequency – wave-number (F-K) domain. In this domain, the converted data can then be filtered based on a range of frequencies. This Bandpass is an exclusion filter that is designed to remove any data outside a defined zone in F-K space. Once filtered, the data are

reverse Fourier transformed back into the time – space domain and contain very little energy outside the range of the original Bandpass filter.

The fourth process in the workflow is a background subtraction. This process applied a running average background subtraction to the dataset. Each trace in the original data set is replaced by the original trace minus the average trace within a window centered on the original trace.

The fifth and final process in the workflow is the AGC or automatic gain control function. It attempts to compensate for signal amplitude attenuation with propagation. The function attempts to average the amplitudes of all the signals in the trace and operates as a sliding window. This process does not preserve the original amplitude information and therefore relative signal strength becomes meaningless. It does, however, greatly improve features that are visible at greater depths. The migration function in this software is not applied to these data because of the limited functionality of the module. Any attempts at applying an appropriate migration would be guess work and did not serve to improve data quality. Following the application of all the processes described in this section, lines of data are processed to produce the final result (Fig. 2.15) that is significantly improved compared to the original raw data.

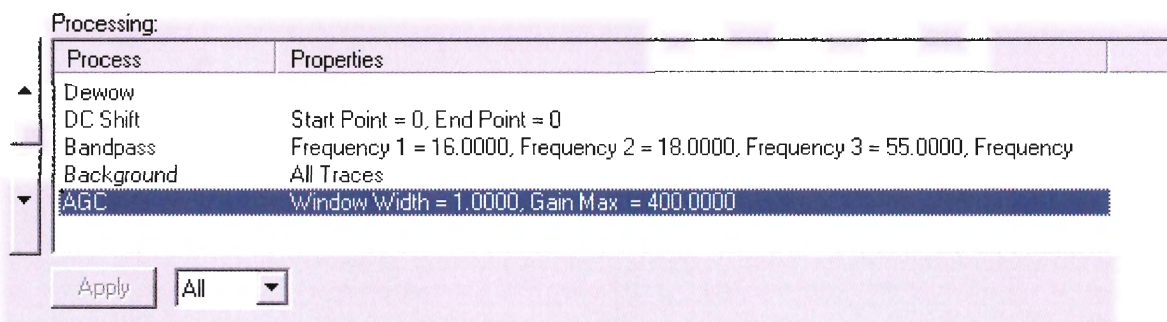


Figure 2.13: Processing window with described workflow. This window is used to apply various processing algorithms to raw GPR data.

After the data processing is complete, the GPR files are exported in SEG-Y seismic format to be adapted for display as profiles in Petrel 2010.

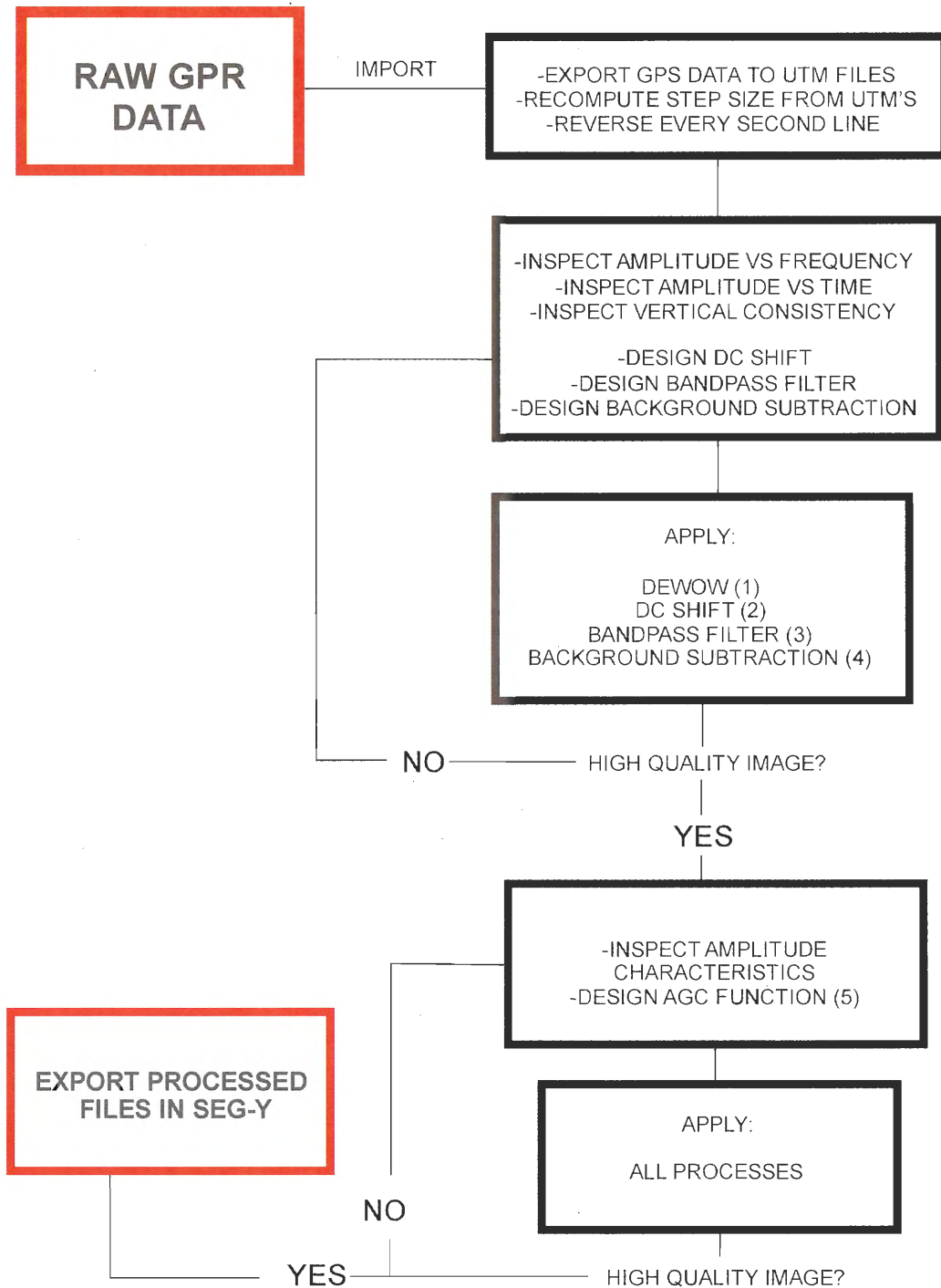


Figure 2.14: Processing workflow for GPR data in EKKO_View Deluxe. Data processing is an iterative procedure that requires a considerable amount of trial and error, particularly with a software package possessing limited data inspection capabilities. Numbers (1) – (5) indicate processing functions.

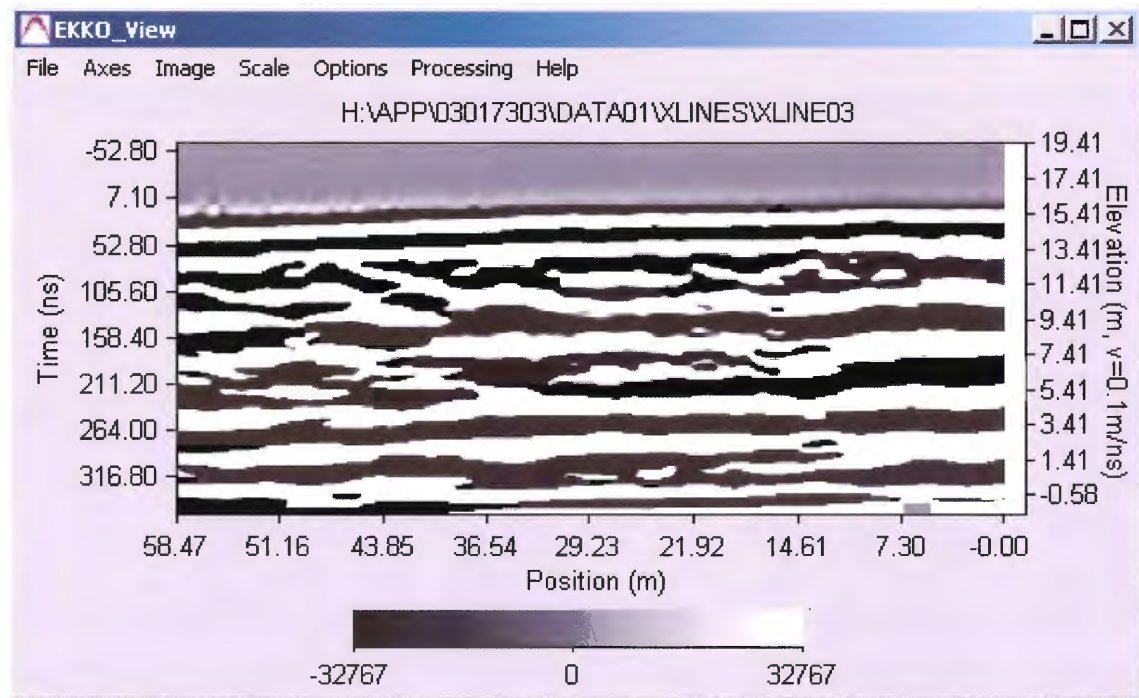
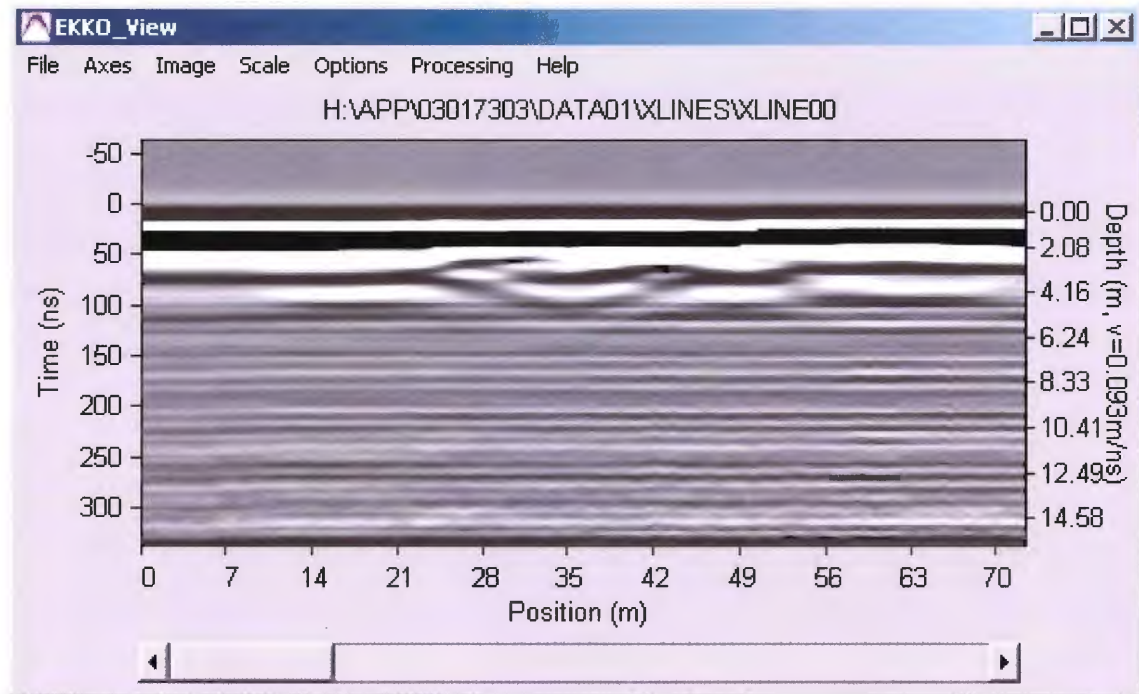


Figure 2.15: Top: Raw GPR data from XLINE00. Bottom: Fully processed GPR data from XLINE03. The processed data reveals topographically, spatially and temporally correct information not apparent in the raw data.

2.4 LiDAR Data

An Optech ILRIS-3D intelligent laser imaging system (Fig. 2.16) was used to acquire an ultra-high resolution 3D point data set in the region of outcrop exposure at Cambridge Cove adjacent to the Minas View golf course and GPR survey location. The data set was acquired by Jordan Nickerson as part of his undergraduate Dalhousie honours thesis work (Nickerson 2010). The 3D point cloud is generated by repeatedly scanning a section of outcrop with the laser, which records range values from the outcrop to the laser with a grid spacing of 5 mm. Each of the millions of range acquisitions is a point with co-ordinates in X-Y-Z space and together, they form a large-scale 3D representation of the surface of the outcrop.



Figure 2.16: Optech LiDAR imaging system at work in the intertidal zone at Joggins. Background: Dalhousie Graduate Adam Fraser. Foreground: Dalhousie Graduate Jordan Nickerson.

The scanner is linked either wirelessly or hardwired to a portable computer which allows the operator to communicate with the scanner and control its operating parameters. The LiDAR starts each scan by generating a grid over a predetermined region of outcrop set by the user as well as simultaneously acquiring high resolution photographs of the same region. It is important to note that the scanner also records the intensity value of the returning laser reflections and assigns each point a grey scale value. It is possible that the intensity of the reflected pulse can be associated with the lithological characteristics of the outcrop. Two overlapping scans were acquired at Cambridge Cove. Each scan comprises several sub-scans which were digitally stitched together to form one composite image (Fig. 2.17).

The LiDAR data sets were post processed using Polyworks, Innovmetric's 3D modeling software. This software is designed to align, edit and view 3D data using a number of sub-modules. The software was used to analyze, align and merge all the sub-scans in each data set, and to smooth the data to render a crisp 3D image. These edited LiDAR data sets are used in this project to define a major component of the 3D framework used to examine the geometries of this braided channel deposit. These data define the bounding edge of the 3D environment and will be used as a correlation surface to map structures from subsurface GPR to LiDAR.

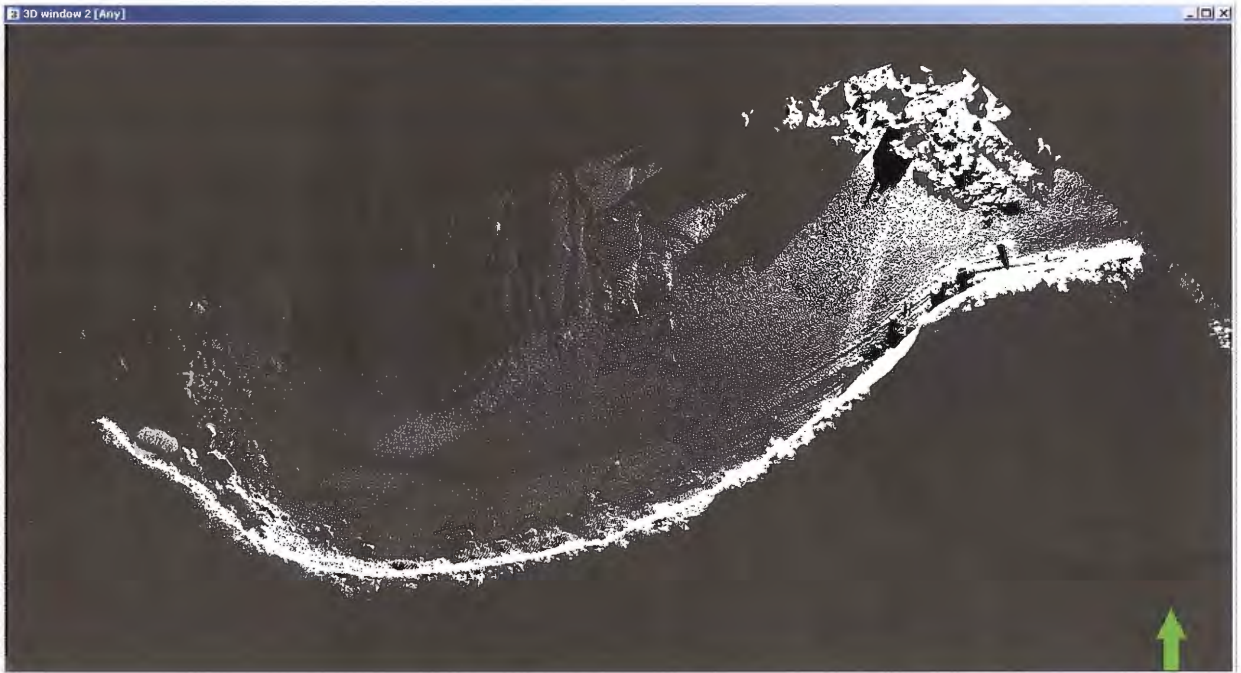


Figure 2.17: Top: Aerial view of study area with LiDAR base location and scanned regions. Bottom: Raw LiDAR data composite in XYZ point cloud format in Petrel 2010.2.

2.5 Construction of 3D Digital Environment

There are two primary components in the development of the 3D digital construct in this study; the GPR data set acquired on the Minas View Golf Course and the outcrop LiDAR data recorded along the cliff face adjacent to the GPR data set. These adjacent data sets and their spatial orientations present ideal conditions for defining the geometry of the braided channel complex.

Before any interpretations could be made, the LiDAR parsing files (ASCII format) that contain both XYZ points and reflectivity intensity values for each of those points were exported from Polyworks and imported into Petrel 2010.2. In order to properly display the data in Petrel, each XYZ point was paired with an attribute value that represented its relative intensity as recorded in the original ASCII file. After assigning a colour scale to the intensity attributes, a high-resolution LiDAR image that is highly representative of the outcrop is produced with stratigraphic horizons, structure and in some instances, lithologic variability (Fig. 2.18).

The next step in construction of this 3D framework involved the integration of processed GPR profiles into the construct. There were a number of challenges that had to be dealt with in order to accomplish this task. In order to integrate the GPR lines into the Petrel environment in a spatially accurate location, the trace headers of all the GPR lines had to be re-written to contain the DGPS coordinates acquired at each trace. Since the trace coordinates and GPR files are stored separately during acquisition, a number of programs were designed in a suite of different programming languages to reformat UTM converted GPS files and write them to the trace headers of the GPR lines.

Since the principal data set with high quality DGPS was acquired during the winter, the GPR cart was modified to run on skis. This meant that the on-board odometer could no longer be

used as either a trigger timer or a distance measurement tool. The GPR cart was instead set to acquire data continuously while simultaneously acquiring DGPS fixes for each trace at the highest possible rate.

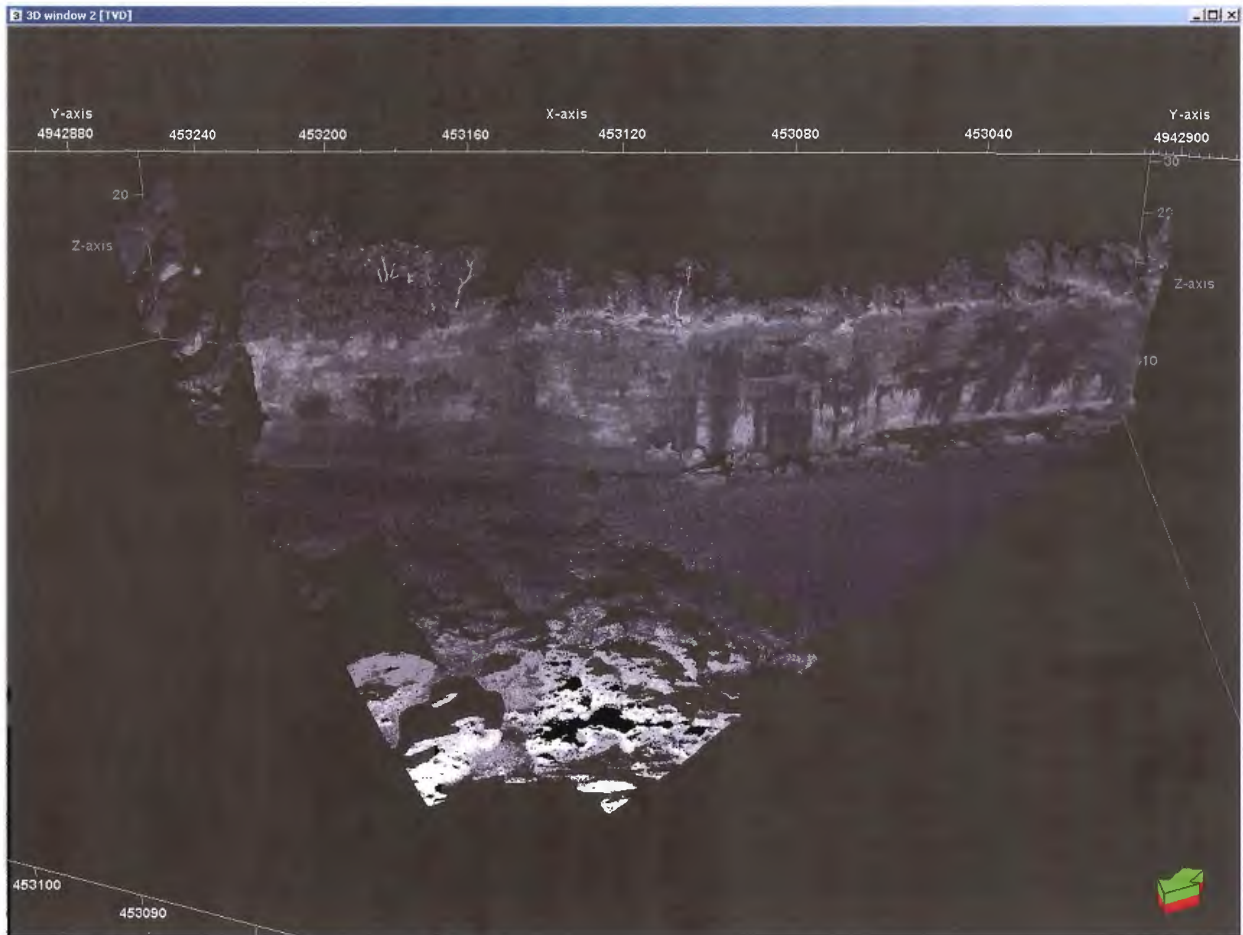


Figure 2.18: LiDAR parsed composite with grey scale as a measure of intensity which has been correlation to lithology. Partially imaged barforms are visible in the intertidal zone (foreground).

However, since GPR data acquisition takes place at a significantly higher rate than DGPS acquisition, the resulting GPR profile contains several sets of traces that contain duplicate DGPS coordinates in their trace headers. Since these DGPS coordinates are used to orient the individual traces in 3D space, the resulting profiles would stack traces coincidentally. In order to solve this problem of duplicate GPS coordinates, every unique UTM coordinate for each profile (Fig. 2.18) was isolated using an AWK script (Script 2.2) compiled in Linux. This script isolates duplicate

GPS coordinates in a text file and deletes them. With the duplicate coordinates removed, a linear interpolation could be constructed to generate unique coordinates for each trace (Fig. 2.19). This linear interpolation was produced by PhD candidate Paul Mattern using a script (Script 2.3) in MatLab. The script first reads the UTM files (Script 2.4) containing the unique coordinates isolated by Script 2.2. It then runs an interpolation to generate new coordinates for each trace and outputs a text file that can be written to the trace headers of each GPR line.

```
$ awk '!a[$3,$4]++' XLINE(xy)_UTM > XLINE(xy)_UTM_UNIQUE
```

Script 2.2: AWK script for removing duplicate UTM coordinates.

```
function interpgpsdata(infile, outfile)

data = textread(infile, '', 'headerlines', 1, 'delimiter', ' ');
newstamp = (data(1,1):data(end,1))';
%remove duplicates
[dump uind] = unique(data(:,2:end), 'rows', 'first');
data = data(uind,:);

% interpolate each column
newdata = nan(length(newstamp), size(data,2));
for icol = 2:size(data,2)
    newdata(:,icol) = interp1(data(:,1), data(:,icol), newstamp,
'linear', 'extrap');
end
newdata(:,1) = newstamp;
figure
hold on
plot(data(:,1),data(:,4), 'bo')
plot(newdata(:,1),newdata(:,4), 'r.')

% write out
fid = fopen(outfile, 'w');
for irow = 1:size(newdata,1)
    fprintf(fid, '%5d %1.2f %13.6f %14.6f %5.2f %4.1f\n',
newdata(irow,:));
end
fclose(fid);
```

Script 2.3: Linear interpolation script produced in MatLab.

```

fcell = lscell('*_UNIQUE');
for k = 1:numel(fcell)
    fprintf(' - processing %s\n', fcell{k})
    interpgpsdata(fcell{k}, sprintf('%s_INTERP', fcell{k}));
end

```

Script 2.4: MatLab batch-job for reading and processing a set of UTM files

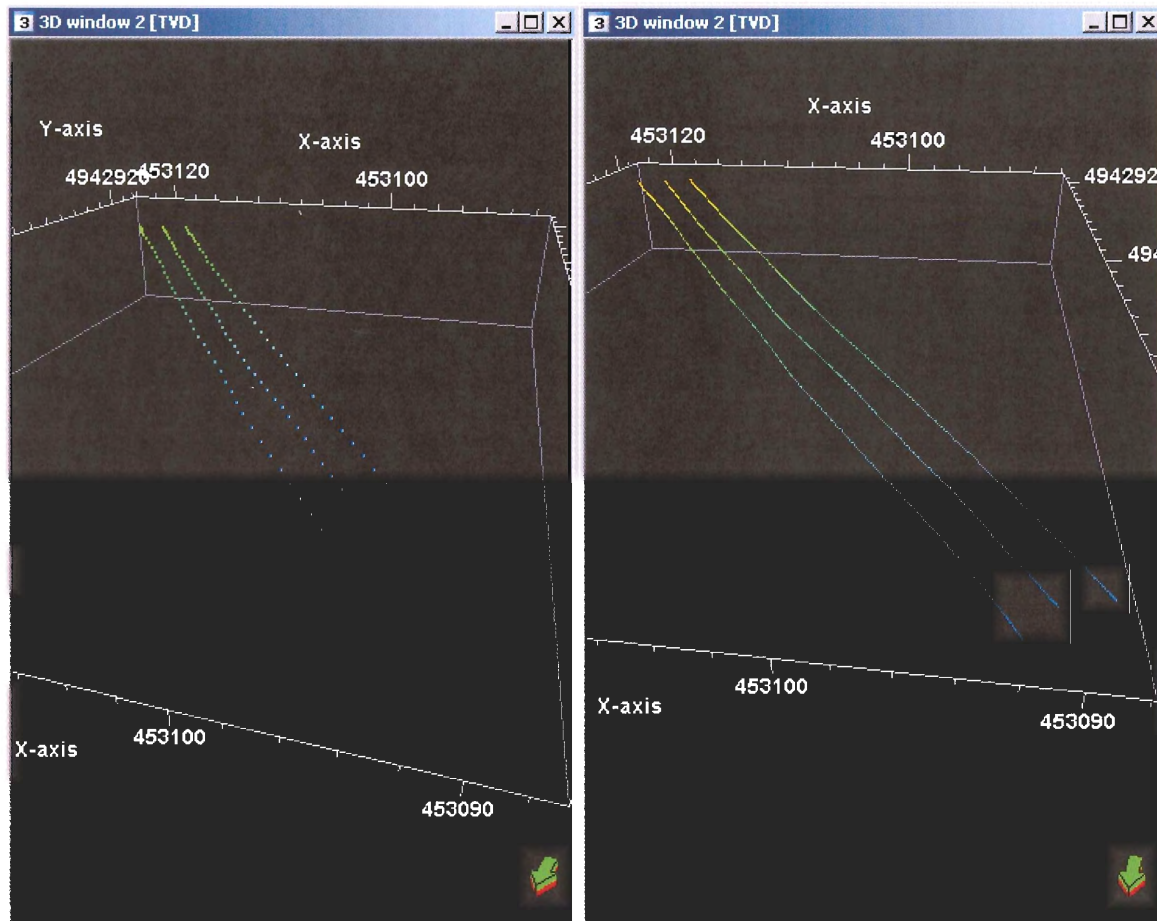


Figure 2.19: Left: Unique isolated UTM coordinates before interpolation. Right: New set of coordinates after linear interpolation.

Once the appropriate navigation data were generated, the next problem to be addressed was to re-write the trace headers of the GPR profiles so that every trace contained a set of unique coordinate data. Solving this problem required the use of advanced programming in C (Compiled by Johnathan Thibodeau, Joanna Gerlings) and led to the development of an original program (Appendix A) designed to re-write SEG-Y format GPR header information in the specific

configuration required for display in Petrel 2010.2. This significant undertaking considered several principles of geophysical data acquisition and was a complex, iterative process (Fig. 2.20).

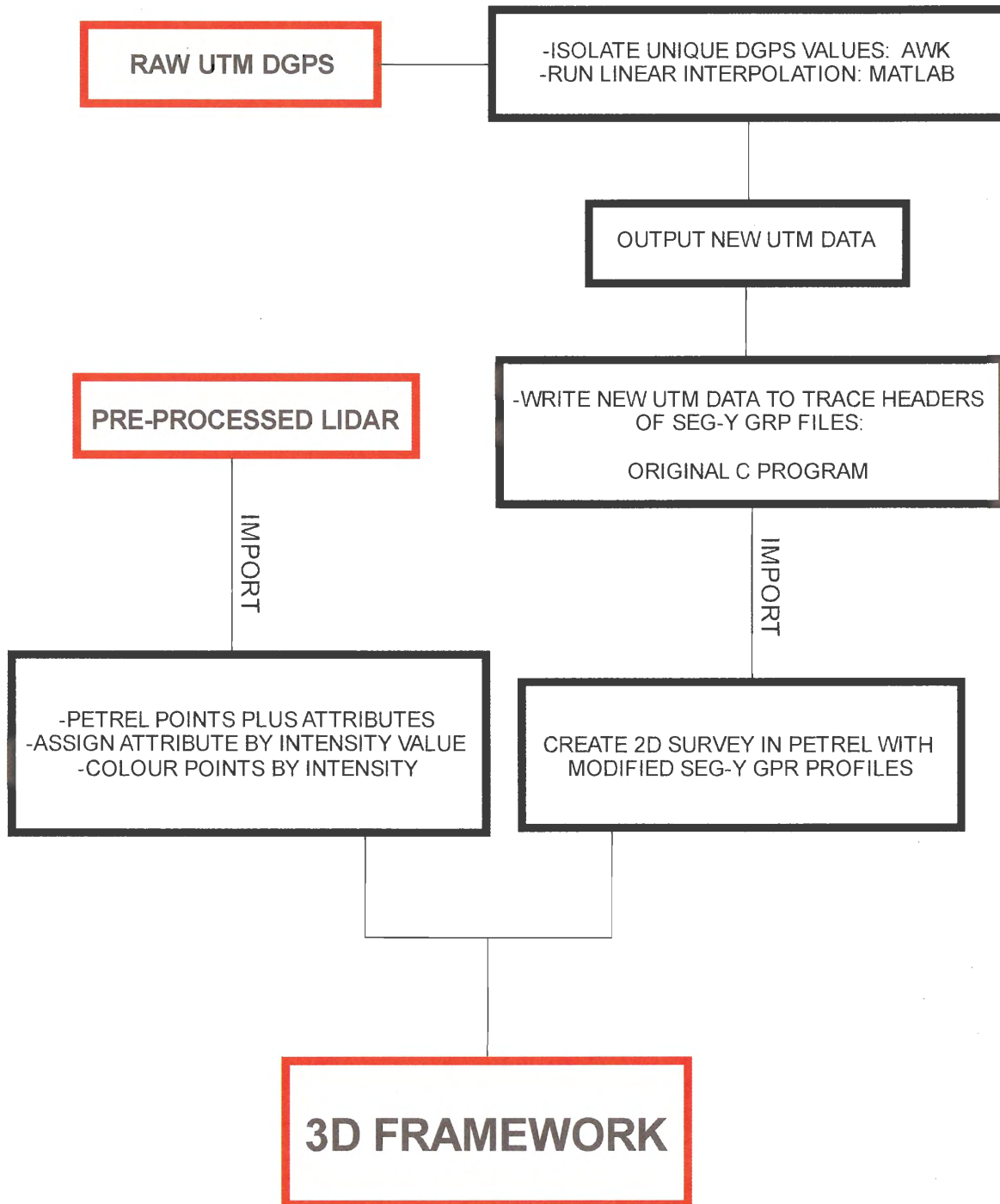


Figure 2.20: Workflow for construction of a 3D, GPR + LiDAR framework in Petrel 2010.2.

The original programming work included in this thesis forms the basis for construction of the 3D digital framework described herein. The program can also be adapted for other GPR data sets with different acquisition parameters and is recommended to be further developed after this project. Once the SEG-Y GPR data had been successfully reformatted, a grid of 2D profiles was generated in Petrel (Fig. 2.21).

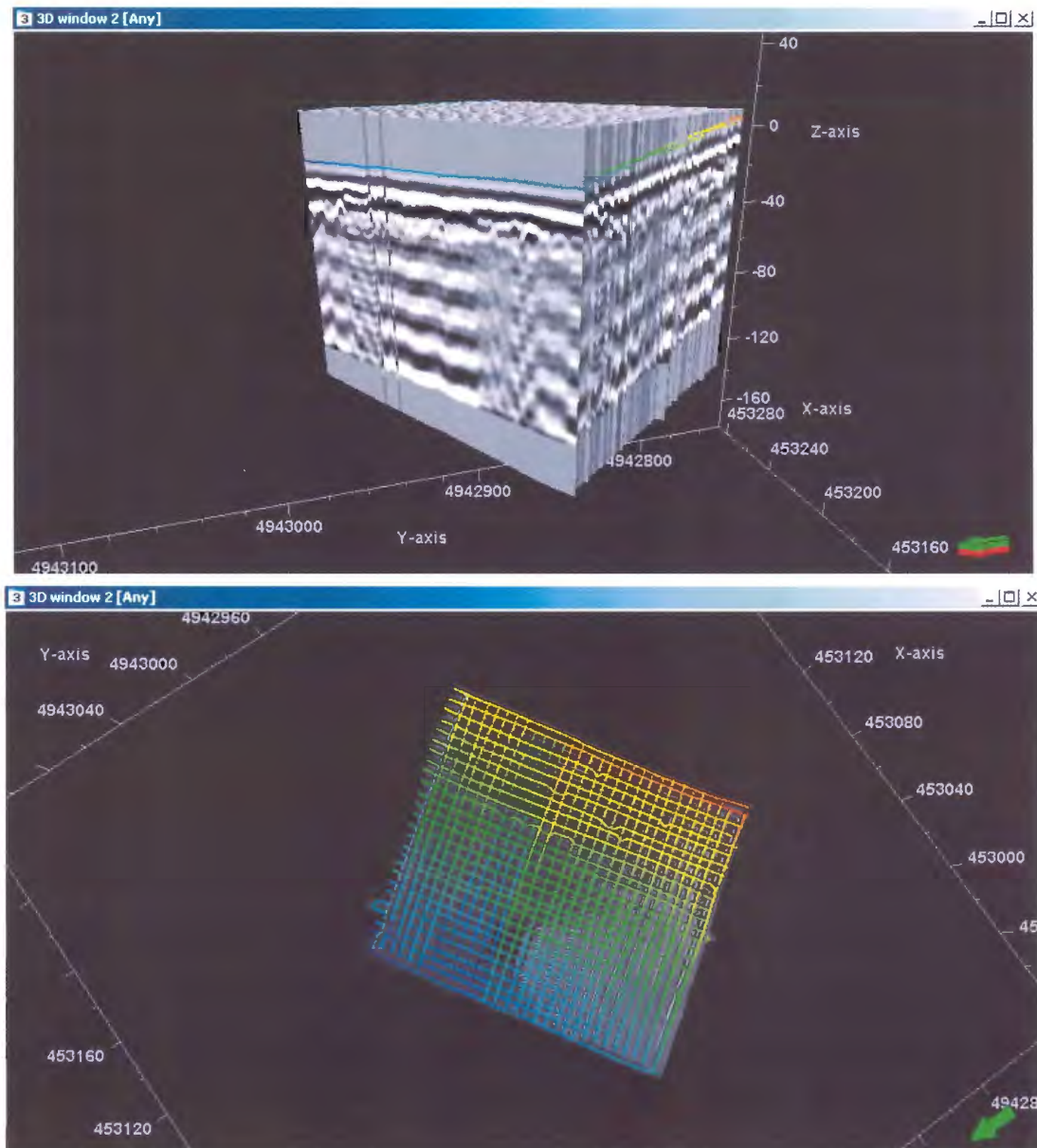


Figure 2.21: Top: 2D GPR X-Y survey grid in Petrel 2010. Bottom: UTM coordinates for GPR survey lines.

Once the technical problems described above were overcome, the resulting environment (Fig. 2.22) of spatially accurate LiDAR and GPR grid data could be displayed, interpreted and mapped to derive subsurface architectural elements in 3D.

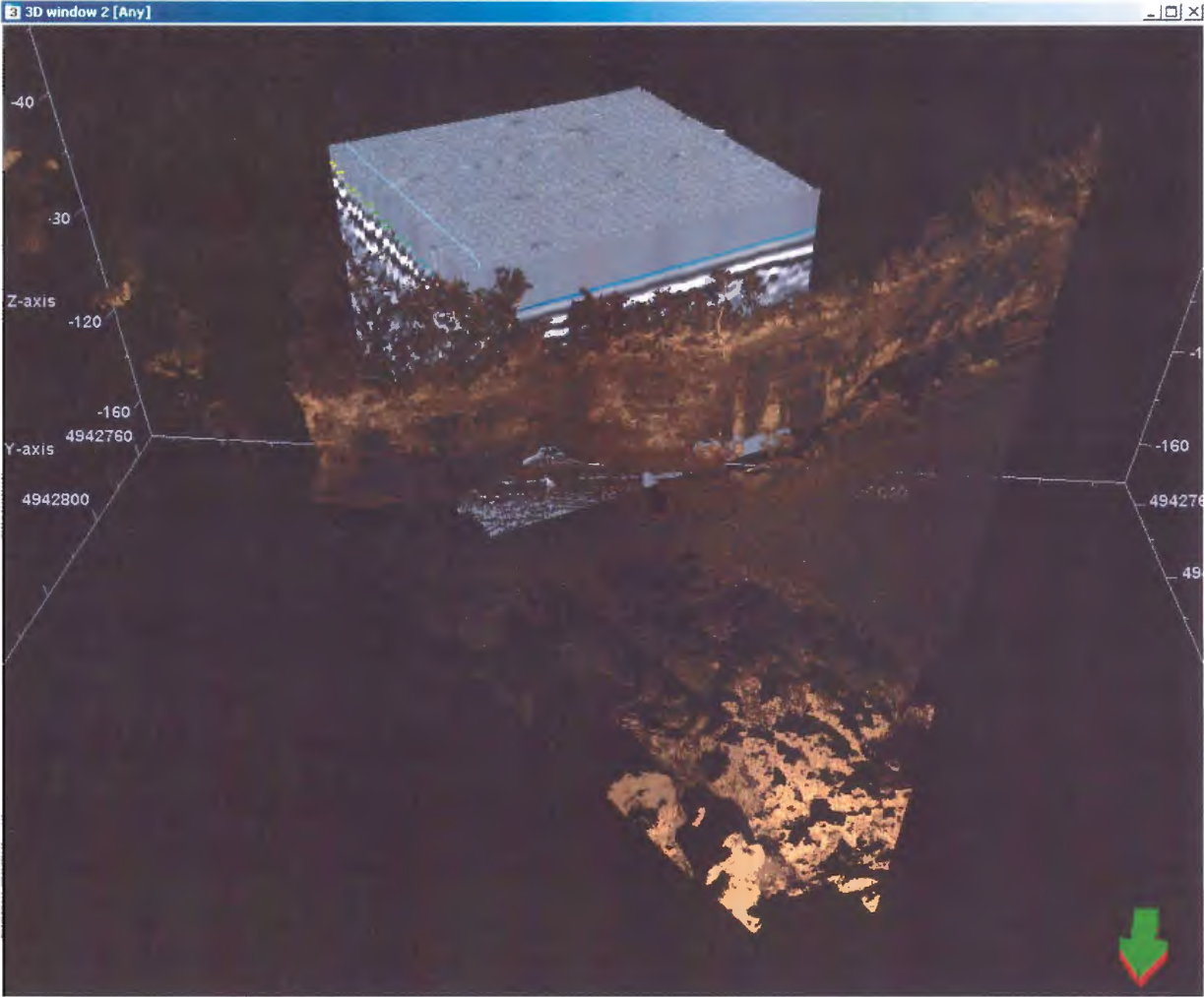


Figure 2.22: Final 3D construct in Petrel 2010 showing LiDAR data (foreground) and the 2D GPR grid survey (background). The spatial proximity of these data sets presents a unique opportunity to explore the detailed architecture of this braided channel deposit at a level of detail not available from outcrop alone. The details visible in the LiDAR image can be identified lithologically by the measured section acquired at this location in 2009. The measured section can also be used to assist in identifying radar facies in the GPR subsurface data. This construct can be used as a tool to map and examine the geology of this section in the third dimension. The programming workflows and methodologies developed to create this construct can be adapted to accommodate any other GPR data set and incorporate it into Petrel for generation of 2D survey grids (Fig. 2.20) and represent a powerful, original visualization tool.

2.6 Mapping of GPR and LiDAR

The 2D GPR grid was interpreted and mapped following the same methodology applied to seismic interpretation. Individual horizons and structures were identified and mapped on a section by section basis in both the X and Y directions to produce grids of intersecting points that define architectural elements. These grids can be interpolated to create continuous surfaces (Fig. 2.23) and fault planes that represent subsurface structures as interpreted from the data.

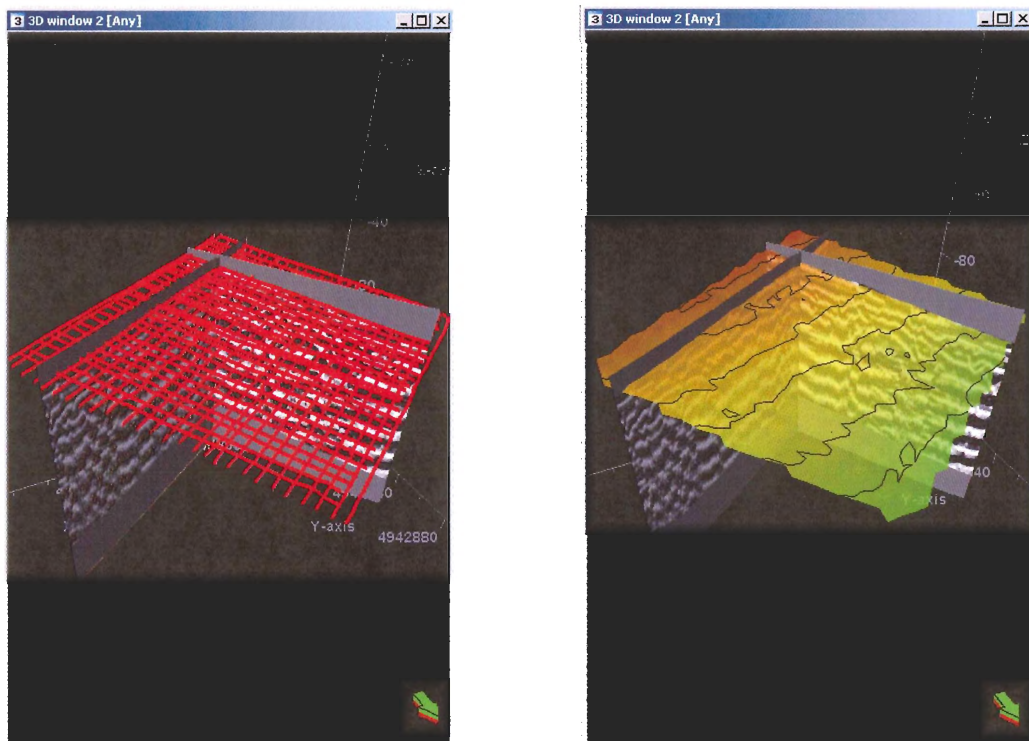


Figure 2.23: Left: Digitized grid of perpendicular lines that represent the mapped location of the surface of the golf course on each individual profile. Right: The surface representation of the ground interpolated from the grid of perpendicular lines.

Mapping of visible structural and stratigraphic features in the LiDAR dataset was conducted by manually digitizing 3D polygons representing stratigraphic boundaries and faults. This process was aided by data from the measured section (Fig. 1.17) from the outcrop. Mapping these features in LiDAR provided a prediction of what features might be present in the adjacent GPR data set.

CHAPTER 3: Results

3.1 Interpretation of GPR and LiDAR

LiDAR Interpretation:

Through interpretation of outcrop photographs, measured sections (Nickerson 2010) and visual analysis of the LiDAR image, several horizons were identified and mapped along the LiDAR dataset (Fig. 3.1 A). Three horizons identified in the measured section (Fig. 3.2) from this portion of the outcrop were identified and manually digitized. By defining the location and shape of these stratigraphic horizons in 3D, it was possible to begin to calibrate these horizons to reflections in the GPR data. In particular, it became possible to groundtruth horizons represented in the GPR dataset and correlate to the adjacent LiDAR derived polygonal representation of the outcrop.

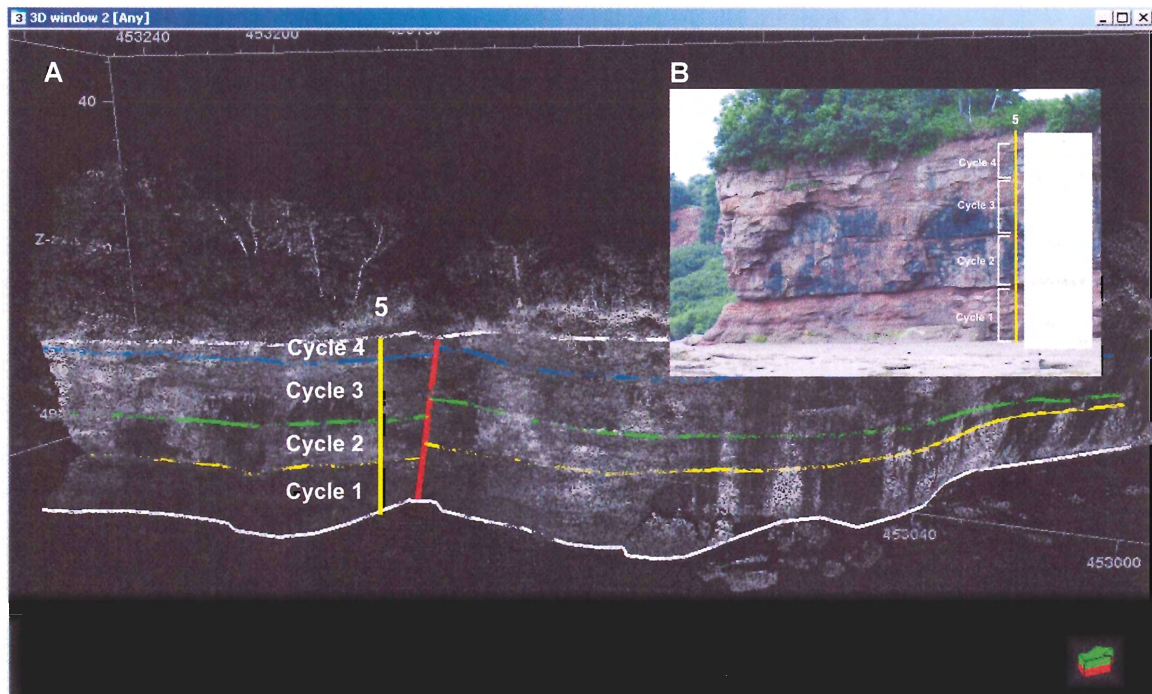


Figure 3.1: A: Horizons mapped to the LiDAR image. This process utilized the combined information from the measured section and outcrop photographs in Fig. 3.1 B with observation of the digital image. The pixilated appearance of the LiDAR image above is a consequence of reducing the point density of the data to 1/10th for ease of image manipulation and to reduce the amount of data shrouding the digitized horizons.

The tops of Unit 1, Unit 2 and Unit 3 from the measured section (Fig. 3.2) were identified in the LiDAR image. Unit 1 represents 4 metres of matrix-supported conglomerates (Figure 3.3) which are separated into two beds by an erosional contact. This unit comprises low-angle, cross-stratified, planar beds with imbricate clasts and is topped by 1 metre of coarse-grained sandstone. Unit 2 is 5 metres thick and begins with a thin bed of matrix-supported conglomerate capped by a sharp erosional scour. This is infilled with clast-supported conglomerates grading upward into matrix supported conglomerates, which is capped by 1 metre of clean, coarse-grained sand. Unit 3 is 4 metres thick and contains two beds of matrix supported conglomerate that fine into coarse-grained sand at the top. Unit 4 is 3 metres thick and starts with the deposition of clast-supported conglomerate in an erosional scour into the top of unit 3. This unit is capped by a matrix-supported pebble conglomerate that contains minor, low-angle cross-stratification in planar beds.

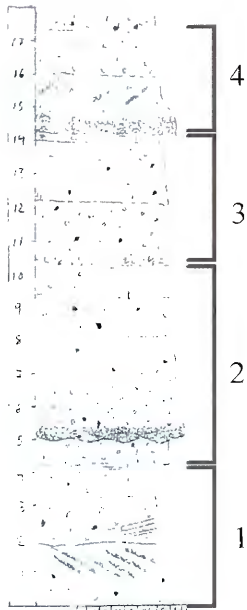


Figure 3.2: Measured section 5, after Nickerson 2010



Figure 3.3: Example of a matrix-supported pebble conglomerate with 5cm lense cap for scale.

GPR Interpretation:

The use of 50 MHz data means that the resolution of the subsurface profiles examined here is limited to larger scale structures like major lithological contacts, faults and the major unconformity between the Wolfville Formation and the Horton Group where electric impedance would be considerable. Smaller scale features such as dunes, barforms and individual channel fills are likely only represented by reflections defining the margins of larger channel fills or barforms. The complex internal geometries of these features can only be properly imaged with higher frequencies in the 150 to 250 MHz range. The higher frequency datasets have been acquired in another section of the golf course (Fig. 2.1), but the GPR information associated with these datasets is of low resolution and requires position error analysis, processing and interpolation and is not incorporated here due to time constraints.

Interpretation of GPR profiles required that a series of radar facies associations be developed upon which to base structural and stratigraphic interpretations. Three unique radar facies were identified in the dataset and their characteristics are outlined in Table 3.1. Visual representations of the radar facies described below are provided in Figure 3.4. A representative profile displaying a number of 2D interpretations is shown in Figure 3.5. Once identified, these facies were mapped throughout the GPR data and several 3D subsurface maps representing horizons and structural features were produced.

Radar Facies	Reflection Pattern	Sedimentological / Structural Interpretation
1	High-angle inclined reflections with associated displacement of adjacent reflections	Faults
2	Low-angle to flat-lying, high amplitude reflections	Lithological contacts or facies changes (plausible cycles identified in measured section and mapped in LiDAR data)
3	Reflections of variable dip enclosed by concave reflections. Chaotic, discontinuous, undulose trough-shaped reflections	Partially resolved channel fills. Partially resolved dunes or barforms. Stacked channel bodies.

Table 3.1: Characteristics of three radar facies (faults are structural features but are referred to here as a facies) identified in the Wolfville Formation conglomeratic braided channel deposit See Figure 3.4 for illustrations.

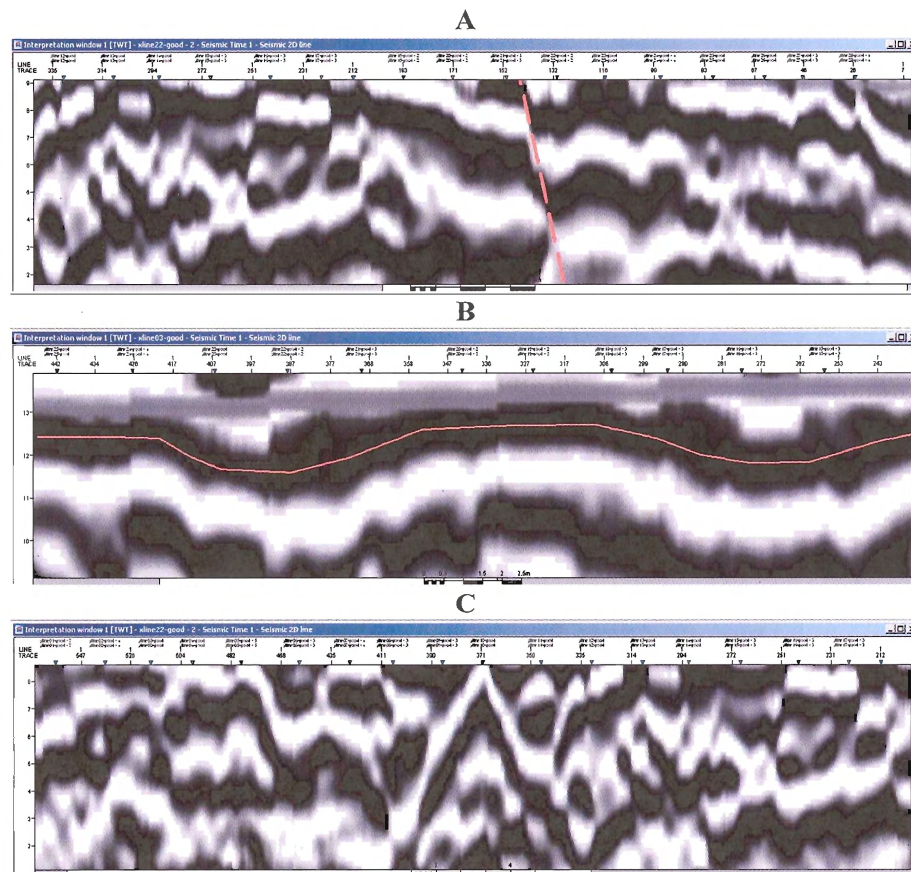


Figure 3.4: Examples of the three identified radar facies described in Table 3.1. A: Radar facies 1. B: Radar facies 2. C: Radar facies 3. Vertical scale is in nanoseconds.

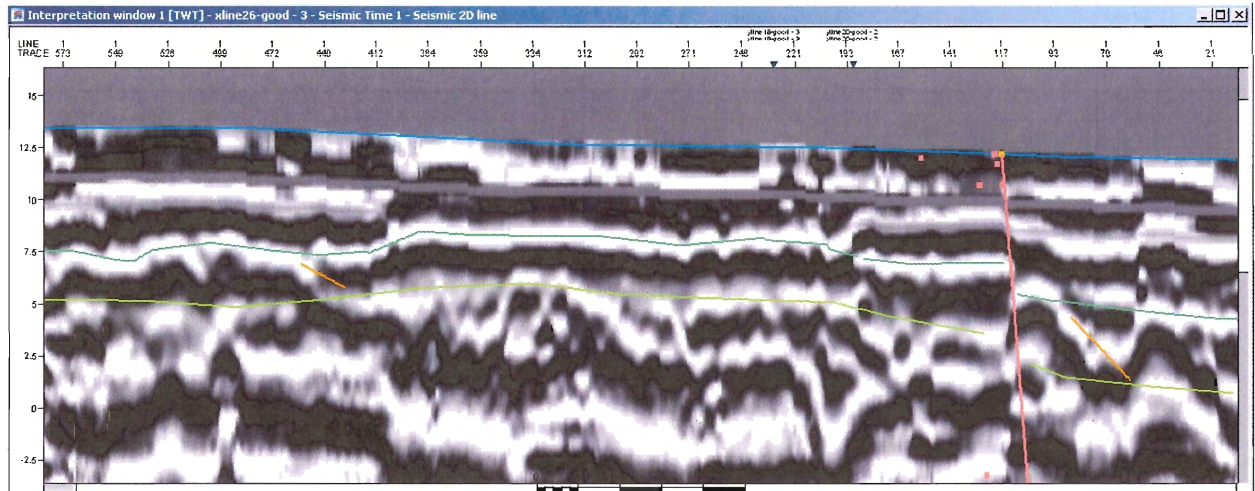


Figure 3.5: A representative GPR profile with a number of interpretations as examples of the facies described in Fig. 3.4 (The blue horizon is interpreted to represent the ground. The aqua horizon is interpreted to represent Top Unit 2. The green horizon is interpreted to represent Top Unit 1. The orange markers are the discontinuously mapped facies 3 reflectors. The red line is interpreted to represent a fault).

3.2 Subsurface Structure Maps

One fault (Facies 1) and three horizons (Facies 2) were identified and mapped throughout the dataset and some preliminary mapping of Facies 3 was conducted. The uppermost horizon (Fig. 3.6) is interpreted to represent the surface of the golf course and is called “GROUND”. The next surface down is interpreted to be the top of Cycle 2 (Fig. 3.7) as identified in LiDAR and on measured section 5. This horizon is called “Top Cycle 2”. The deepest horizon mapped (Fig. 3.8) is interpreted to represent the top of Cycle 1 (Basal cycle) as identified in LiDAR and on measured section 5. This horizon is called “Top Cycle 1”. The fault (Fig. 3.9) is interpreted to represent the fault identified and mapped in the LiDAR data and in outcrop photographs and is referred to as “Fault L” for LiDAR.

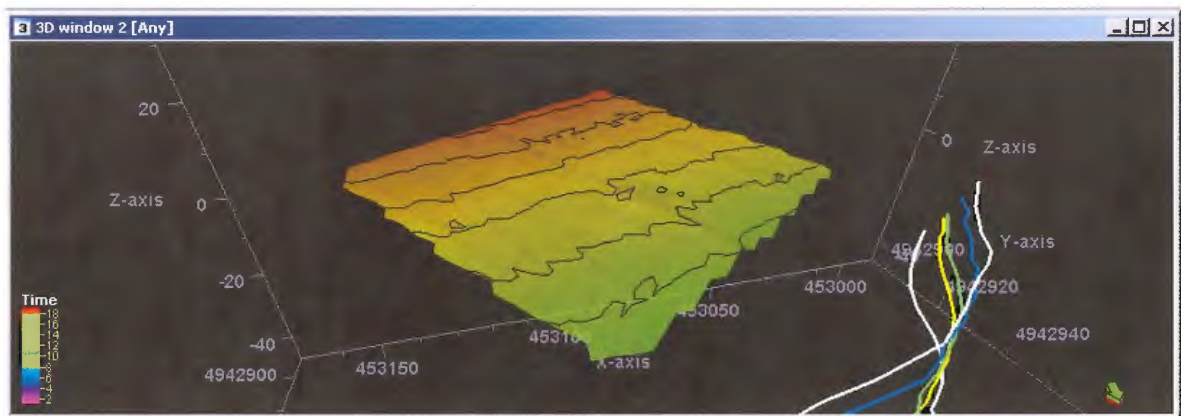


Figure 3.6: Horizon “GROUND” representing the surface of the golf course (Time is scaled to depth in metres). This surface correlates to the upper white LiDAR polygon.

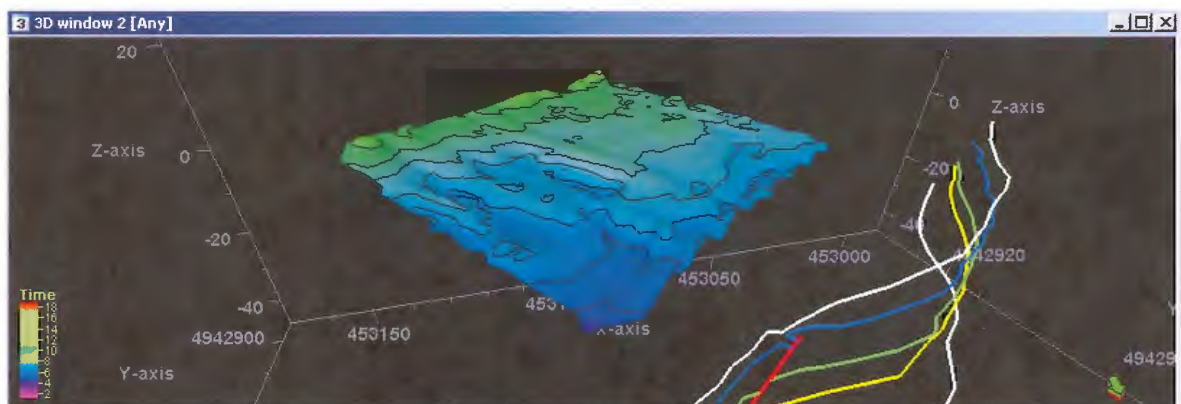


Figure 3.7: Horizon “Top Unit 2” (Time is scaled to depth in metres). This surface correlates to the green LiDAR polygon.

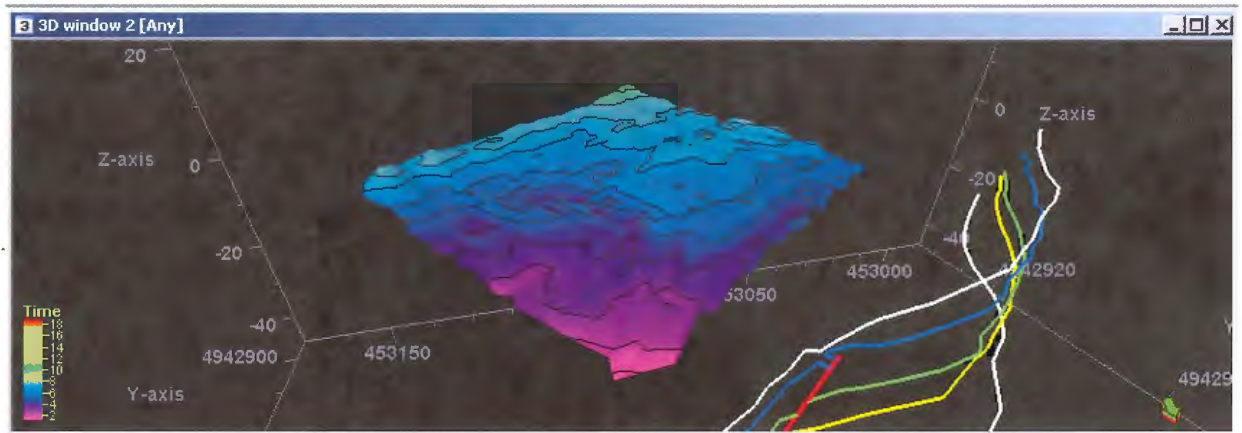


Figure 3.8: Horizon “Top Unit 1” (Basal cycle, time is scaled to depth in metres). This surface correlates to the yellow LiDAR polygon

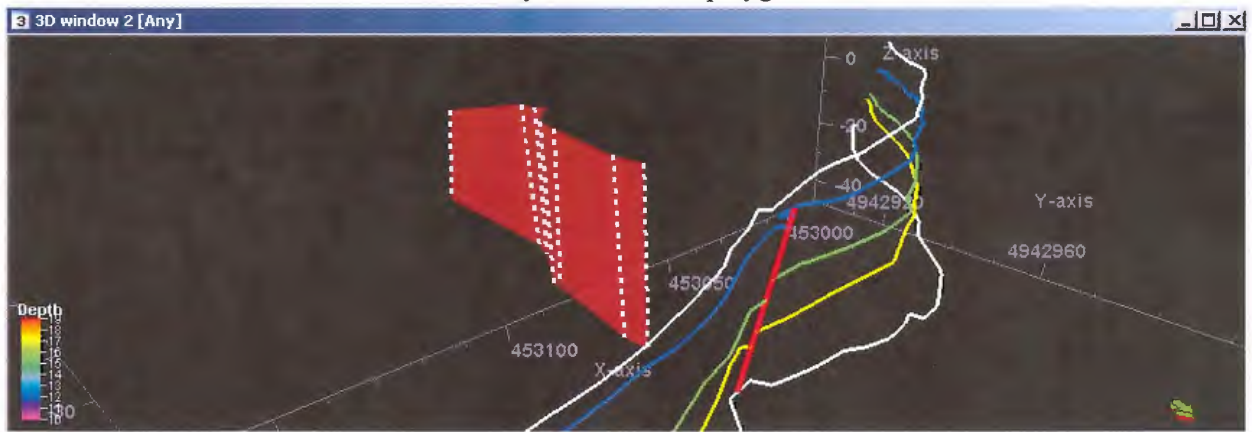


Figure 3.9: Structure “Fault L”. This fault tips out in the middle of the dataset and decreases in throw with distance from the outcrop. This feature correlates to the red LiDAR polygon.

The fault identified in Figure 3.9 offsets the horizons Top Unit 1 and Top Unit 2 with a maximum amount of displacement of $\sim 2\text{m}$ at the outcrop and with decreasing offset to the south until tipping out $\sim 40\text{m}$ to the south of the cliff. Unit 2 thins to the southwest and thickens in the direction of paleo-flow to the north as confirmed by both outcrop LiDAR and subsurface maps. Both the top and base of Unit 2 show evidence of scoured contacts in the form of their irregular surfaces which dip gently to the north. This irregularity is particularly evident at the base of Unit 2, corresponding to the erosional contact identified in the measured section.

The upper 5 metres of the GPR dataset is masked by very high amplitude responses from the direct and airwaves, obscuring any potential reflections from the shallow top of Unit 3. The

deeper section of the dataset, below a depth of 12-15 metres, is dominated entirely by ringing noise not removable from the data given the level of sophistication of the available processing software. Therefore, no mappable horizons were visible greater than 1-2 metres below the horizon Top Unit 1. Consequently, there remains only a limited section of interpretable data.

Preliminary mapping of Facies 3 reflections was conducted on the volume contained within the Top Unit 1 and Top Unit 2 horizons, which is interpreted to represent Unit 2. This region of the dataset contains several occurrences of chaotic or discontinuous reflections that are frequently bound by steeply dipping, moderate amplitude reflections that cut across Unit 2. These reflections are interpreted to represent either the margins of larger barforms or channel fills. The reflections were identified and digitized in a discontinuous fashion (Fig. 3.5) and therefore much of the low relief regions on the resulting surface are derived by interpolation. The high relief features are, however, constrained by digital picks. Mapping was conducted with the knowledge that a surface generated from the reflections was discontinuous due to the nature of the radar features being mapped.

The resulting horizon named “Unit 2 Architecture” (Fig. 3.10) exhibits features interpreted as elongate, rhomboid-shaped barforms separated by channels. In some cases, the barforms show directional trends that correlate to the northerly paleo-flow directions indicated by exposed barforms in the intertidal zone. This map reveals information about the internal architecture of the Unit 2 package, providing data that can be applied to understanding subsurface reservoir characteristics (Section 4.1).

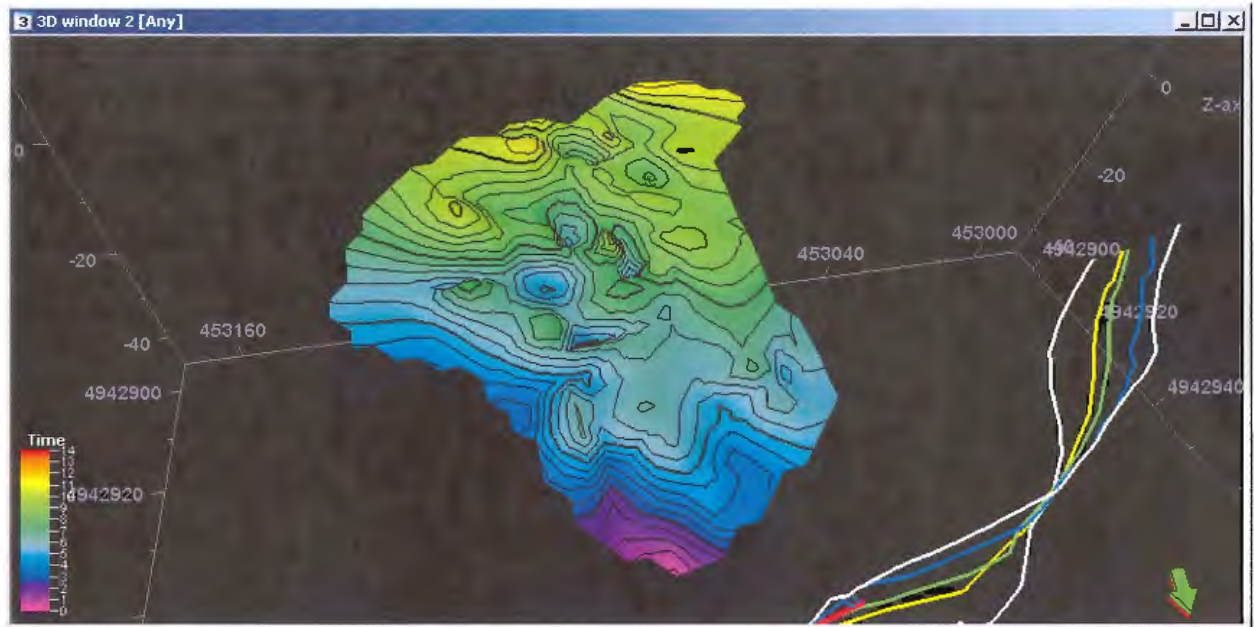


Figure 3.10: Horizon “Unit 2 Architecture”. Several of the features observable on this subsurface map resembles the 3D barform exposures visible in the intertidal zone. Some features are elongate in the direction of paleo-flow and have rhomboid geometry, representative of barforms. The shape of the horizon is a consequence of digitizing a boundary around the interpreted region to avoid edge distortions and extrapolation beyond the available data when interpolating the final surface geometry (time is scaled to depth).

When combined, the features identified above form the 3D subsurface architecture of this region of the braided channel that can be calibrated to the adjacent outcrop (Fig. 3.11). The GPR and LiDAR datasets have been processed, integrated, interpreted, mapped and correlated to reveal subsurface information.

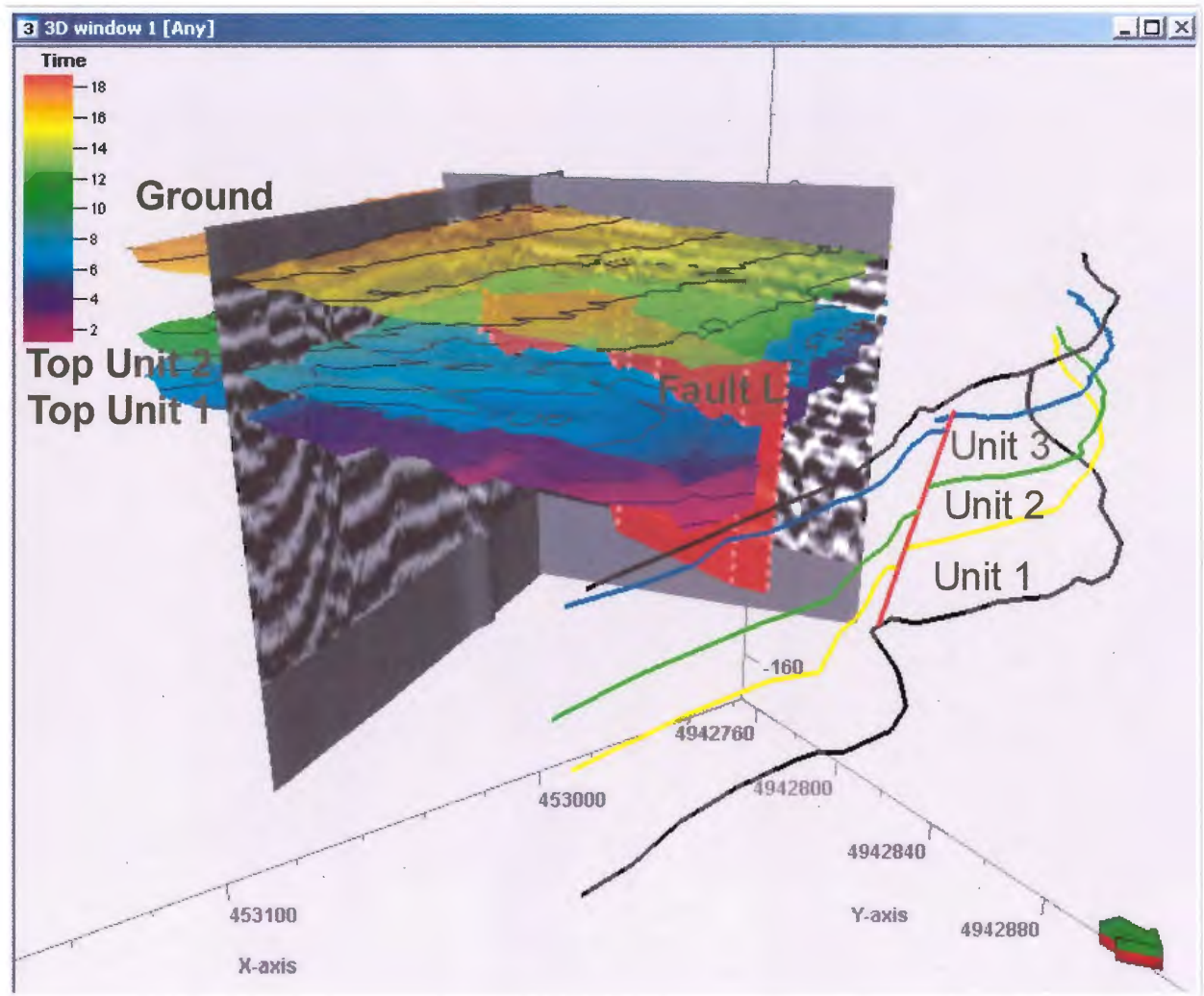


Figure 3.11: Complete 3D subsurface stratigraphic and structural map with some GPR lines for reference (For viewing clarity, Unit 2 Architecture is omitted from this diagram and the horizon GROUND has been made partially transparent, time is scaled to depth equivalent in metres). The features mapped in the GPR dataset are correlated to the adjacent outcrop LiDAR image, forming a comprehensive construct that delineates the subsurface architecture of this region of the deposit in 3D (Time is scaled to depth).

CHAPTER 4: Discussion

4.1 Reservoir Characterization

Through interpretation of outcrop field observations, measured sections, high-resolution photographs and LiDAR data, major channel bodies and barforms were previously identified and mapped in the cliff face along the section (Nickerson 2010). With new structural and stratigraphic information derived from GPR mapping, further interpretations can be made about the Wolfville Formation and its characteristics as a reservoir.

Correlative strata have been derived from horizons “Unit 2 Architecture” by examination of the surface relief. By applying braided channel geometry discerned from the 2D and 3D outcrops to the structure map, the bar-forms and channel fills can be interpreted (Fig. 4.1). The depositional system contains divergent and convergent channels, barforms and confluence and constriction scours (Fig. 1.15, Gibling 2006); all characteristic features of a channelized fluvial depositional environment. These observations correlate with outcrop lithology maps for Unit 2 and identified in Figure 4.2, which indicate the presence of barforms (matrix-supported conglomerates) above channel bodies (clast-supported conglomerates), capped by medium-to-coarse grained sandstone beds.

Compartmentalization of this reservoir analogue is controlled by baffles and barriers to flow. These include structural components such as faults and stratigraphic vertical and lateral permeability contrasts. We can address the controls on fluid flow within this braided channel complex and identify the key factors in compartmentalization of fluids within this reservoir by examining these components.

The permeability of these lithologies (Table 4.1) were previously recorded in this location by Nickerson (2010) using an outcrop permeameter (Tiny Perm). Fluid flows readily

within the clast-supported conglomerates that comprise the channel bodies (Nickerson 2010). The permeability of the matrix-supported conglomerates that comprise the barforms is less than that of the channel bodies in part due to spaces between clasts being filled with medium-to-coarse grained sandstone. The medium-to-coarse grained sands that cap the cycle are less permeable than the dominant conglomerates because of smaller pore spaces and decreased connectivity between pores. The thin paleosols that form the base of Unit 2 are assumed to have the lowest permeability values as they comprise fine-grained sandstone with minor silt and carbonaceous materials attributed to rooting (Nickerson 2010). Thus, the fining-up nature of the cycle is reflected in the decreased permeability values. It should be noted that the permeability data may not correspond to the actual permeability of the subsurface behind the cliff face, as surface weathering has occurred along the face of the outcrop, dissolving the calcite cement contained within the rock.

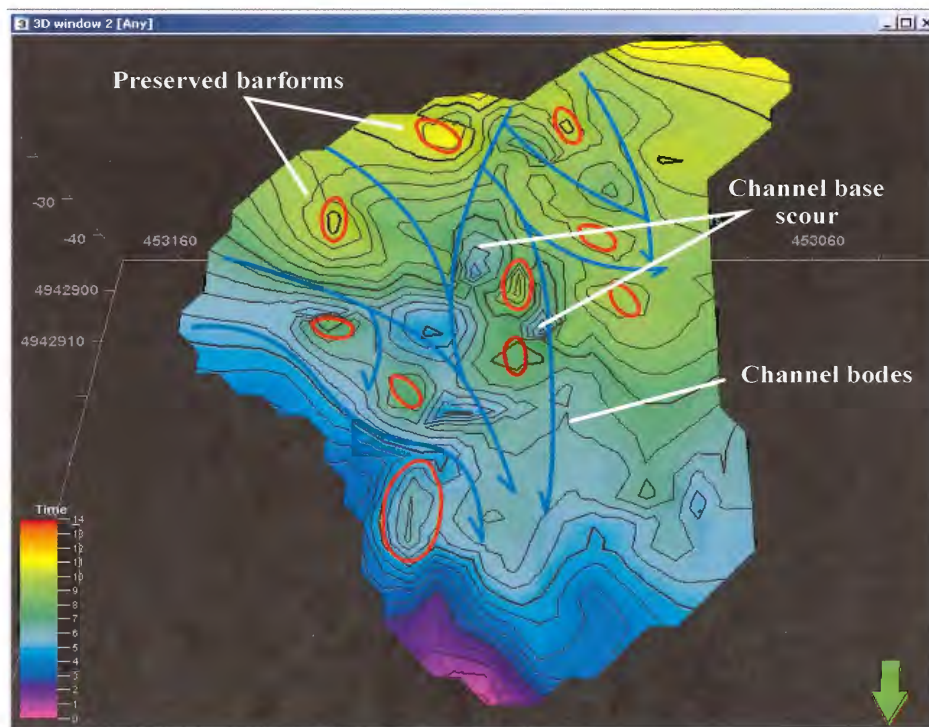
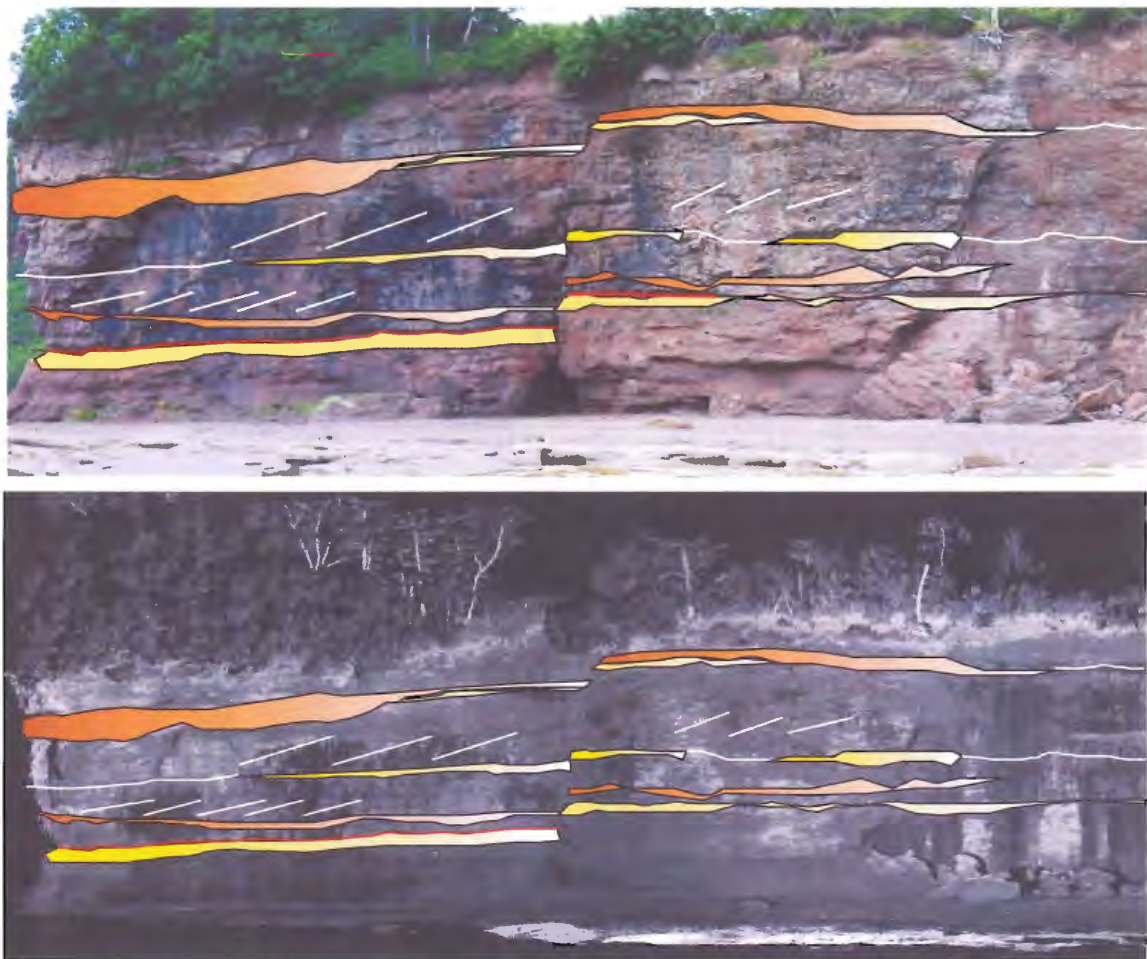


Figure 4.1: Superposition of braided channel geometry on the Cycle 2 Architecture horizon. The locations of preserved barforms, channel bodies and channel base scours are hypothesized.

The results obtained from the high-resolution photogrammetry and LiDAR (Nickerson 2010) identified the lateral extent of the various lithofacies and the internal architectural elements visible in the exposed outcrop (Fig. 4.2). It was found that clast- and matrix-supported conglomerates dominate the outcrop section. Some beds contain preserved channels that have been infilled with clast supported conglomerate whereas the large bedforms are laterally continuous.







Color	Lithofacies	Architectural elements	Width	Thickness
	1	Channel Bodies	>50m	<1m
	2	Barforms	>100m	<3m
	3	Medium-Coarse Grained Sandstone Beds	>100m	<1m
	4	Paleosols	>50m	<0.5m

Figure 4.2: Lithofacies identification in outcrop and LiDAR after Nickerson, 2010.

Facies No.	Height	Permeameter value	Permeability (mD)
3	18 metres	11.32	70mD
2	12.5 metres	10.76	350mD
1	7metres	10.49	800mD

Table 4.1 Lithofacies permeability obtained from measured section 3 (Nickerson 2010).

The structural features observed within the cliff face can further add to the compartmentalization of the reservoir by offsetting stratigraphically connected bedforms and channel fills with variable permeability lithofacies. Offset along fault planes can lead to the juxtaposition of high and low permeability facies, creating a baffle to flow and diminishing the horizontal communication with the reservoir. Fault seal can also impact permeability, for example, Fault L in the section is assumed to be a sealing fault that does not permit horizontal fluid flow. This assumption is backed by the high amount of calcite found within the faults and the lack of water seeping across the fault planes, suggesting that there was migration of meteoric water vertically along the fault surface and sealing during diagenesis (Nickerson 2010). Structural features such as faults can also, in some cases, serve to increase vertical fluid flow within the reservoir by creating vertical migration pathways, particularly during tectonic events that initiate fault motion.

Fluids within this type of reservoir would tend to migrate horizontally through the large scale barforms and occupy channel bodies preferentially due to the higher permeability of the conglomerates vs. the sandstones and paleosols that confine Unit 2. Most of the cycles identified

in this outcrop are capped by lower permeability lithofacies, thus creating baffles and possible barriers to vertical fluid migration, depending on the fluid type. This type of fluid flow creates stratigraphic reservoir compartmentalization, as the effective drainage of the reservoir is now diminished by creating pockets of fluid trapped within highly permeable lithofacies, capped by baffles and barriers of low permeability lithofacies and laterally contained by non-transmissive faults. With the higher resolution GPR datasets, it is recommended in a future project to map and isolate channel fills from stacked barforms and sandstone beds to develop a high resolution subsurface reservoir model to simulate fluid and gas flow.

In Atlantic Canada, several basins with excellent reservoir/seal pairs are candidates for the geological storage of CO₂ in either a liquid or a gas phase (Wach et al. 2010). Seal, storage capacity and economic feasibility are the most important components of the CO₂ geologic sequestration system. For example, hydrodynamic seals carry a greater associated risk than cap-rock or membrane seals. Storage capacity is a function of porosity and permeability, lateral reservoir continuity, the regional and local stress fields and the effect CO₂ injection will have on the reservoir over time. By developing detailed reservoir characterizations and modelling analogue reservoirs in outcrop using methodologies like those described in this thesis, it is possible to evaluate analogue subsurface sites like the Wolfville Formation deposit for ranking as a possible sequestration site for CO₂, an important and promising prospect for long term management of waste carbon emissions.

4.2 Methodology Recommendations

Several factors influence the quality of geophysical datasets. The exposures and geometry of the survey environment at Cambridge Cove presents a rare opportunity to work with subsurface data because of the added benefit of being able to correlate and ground-truth subsurface features without any well data. The adjacent outcrop and intertidal zone is easily accessible, thoroughly studied and provides an excellent 2D and 3D representation of what the GPR survey is targeting. The ground cover in the survey area is grassy and there are no known subsurface obstructions such as irrigation pipes or current-carrying wires. We have a well established rapport with the owners of the property, who provide access to the site and the use of their carts to move equipment and people around the site.

In this project, however, there were a number of unusual circumstances with potential to impact geophysical data acquisition. Snow cover, potential interference from the skis attached to the cart, continuous data acquisition at relatively high rate, cold temperatures and partially frozen subsurface contributed to data quality.

In an ideal environment, there would be no cover of any kind, along with flat-lying homogeneous strata with sharp contacts and high electric impedance between each individual layer in the subsurface. These surface acquisition conditions are rarely found. It follows that one would anticipate GPR data acquired from a deposit like the Wolfville Formation to suffer considerable degradation. This braided channel deposit is extremely heterogeneous, with low-angle barforms with irregular contacts between like lithologies, lateral and vertical variation in lithological characteristics and steeply dipping faults with thin till and top-soil cover.

The acquired data exhibited noise and could have benefitted from more refined processing techniques. The higher frequency data sets are better equipped to handle

heterogeneities in the subsurface and will likely yield higher quality data that can be explored in detail in the future. It is not beyond the capabilities of GPR to image this type of deposit, but it is a challenging environment to produce accurate images with GPR. In order to produce quality datasets in the future, a number of methodology considerations are being revisited with respect to survey design. Lessons learned during this research project will serve to contribute significantly to quality data acquisition in the future.

CHAPTER 5: Conclusions

The application of Ground Penetration Radar survey techniques to image the subsurface architecture of the Wolfville Formation braided channel deposit has identified three horizons and one fault in the subsurface. The development of a 3D construct in which to examine the data has allowed for 3D interpretation and mapping and the development of a digital subsurface architecture. The elements of this architecture have been correlated to outcrop on measured sections, outcrop photographs, and digitally mapped LiDAR data. Subsurface maps have revealed the presence of erosional contacts, preserved barforms, channel fills, and scour features commonly observed in modern braided channel environments.

Generation of a 3D visualization construct led to the development of several original methodologies for GPR data processing, DGPS coordinate processing and SEG-Y file header manipulation. An original piece of C programming (Appendix A) was developed and applied to the data in order to properly hang GPR profiles in 3D space in the X, Y and Z directions. Several considerations of survey design have been carefully evaluated during this process and will aid in data acquisition in the future.

The information derived from this comprehensive examination has been used to evaluate the deposit as a reservoir analogue. Permeability values of the lithofacies address the nature of fluid flow within this simulated subsurface reservoir. Structural and stratigraphic reservoir compartmentalization was investigated and it was concluded that fluid flow in this reservoir would be dominated by lateral migration from lower to higher permeability facies, except where calcified faults form barriers to flow. Vertical fluid flow is limited by reservoir baffles and barriers generated by low permeability lithofacies capping depositional units.

6.0 References

- Baker, P.L., (1991). *Response of ground-penetrating radar to bounding surfaces and lithofacies variations in sand barrier sequences*. Exploration Geophysics 22, pp. 19–22.
- Daniels, D.J., (1996). *Surface-penetrating radar*. Institute of Electrical Engineers, London.
- Davies, N.S., Gibling, M.R., (2011). *Pennsylvanian emergence of anabranching fluvial deposits: the parallel rise of arborescent vegetation and fixed channel floodplains*. In: Abstract Volume, Atlantic Geoscience Colloquium 2011, Fredericton, NB.
- Gibling, M.R., (2006). *Width and thickness of fluvial channel bodies and valley fills in the geological record: a literature compilation and classification*. Journal of Sedimentary Research, 2006, v. 76, 731-770.
- Hubert, J.F., (1984). *Eolian sandstone in upper Triassic-lower Jurassic red beds of the Fundy basin, Nova Scotia*. Journal of Sedimentary Petrology, Vol. 54, No. 3, September, 1984, p. 798-810.
- Jol, H.M., Smith, D.G., (1991). *Ground penetrating radar of northern lacustrine deltas*. Canadian Journal of Earth Sciences 28, pp. 1939-1947.
- Leleu, S., Hartley, A.J., Williams, B.P., (2009). *Large-scale alluvial architecture and correlation in a Triassic pebbly braided river system, lower Wolfville Formation (Fundy basin, Nova Scotia, Canada)*. Journal of Sedimentary Research, 2009, v. 79, 265-286.
- Neal, A., (2004). *Ground-penetrating radar and its use in sedimentology: principles, problems and progress*. Earth Science Reviews, Vol. 66, Issue 3-4, pp. 261. Elsevier Publishing, Amsterdam.
- Neal, A., Roberts, C.L., (2000). *Applications of ground-penetrating radar (GPR) to sedimentological, geomorphological and geoarchaeological studies in coastal environments*. In: Pye, K., Allen, J.R.L. (Eds.), Coastal and Estuarine Environments: Sedimentology, Geomorphology and Geoarchaeology. Geol. Soc. London Spec. Publ. 175, pp. 139– 171.
- Nickerson, J., (2010). *Architecture and geometry of braided channel complex in the Triassic Wolfville formation*. Undergraduate Honours Thesis, Department of Earth Sciences, Dalhousie University, Halifax, Nova Scotia.
- Olsen, P.E., (1990). *Tectonic, climatic, and biotic modulation of lacustrine ecosystems—examples from the Newark Supergroup of eastern North America*. In Katz, B.J., ed., Lacustrine Exploration: Case Studies and Modern Analogues: American Association of Petroleum Geologists Memoir 50, p. 209-224.

- Plewes, A.I., Hubbard, B., (2001). *A review of the use of radio-echo sounding in glaciology*. Progress in Physical Geography 2001. Vol. 25, Issue 2, pp. 203-236.
- Prothero, D.R., Schwab, F., (2004) *Sedimentary geology: an introduction to sedimentary rocks and stratigraphy*. 2nd edition. Pp. 315-320. W.H. Freedman and Company, New York.
- Reynolds, J.M., (1997). *An introduction to applied and environmental geophysics*. Wiley, Chichester. Pp. 26-30.
- Sambrook, S.G.H., Ashworth, P.J., Best, J.L., Woodward, J., Simpson, C.J. (2006). *The sedimentology and alluvial architecture of the sandy braided south Saskatchewan river, Canada*. Sedimentology 53, 2006, 413-434.
- Sensors and Software Inc (1999). *Practical processing of GPR data*. Operations Manual.
- Sensors and Software Inc. (2006). Technical Manual: *PulseEKKO Pro User's Guide*. Sensors and Software Inc., Ontario.
- Skelly, R.L., et al.(2003). *Architecture of channel-belt deposits in an aggrading shallow sandbed braided river: lower niobrara river, northeast Nebraska*. Sedimentary Geology 158, 2003, 249-270.
- Wach, G., (2009). *Cambridge-Pembroke-Walton field traverse*. EARTH 3303 Stratigraphy Field Excursion Manual, Dalhousie University. pp. 1-6.
- Wach, G.D., Zentilli, M., Pothier, H.D., (2010). *Assessment of prospective sites for the geological storage of CO₂- Nova Scotia*. Dalhousie University Earth Sciences Department, Halifax, Nova Scotia. April 2010.
- Wade, J.A., Brown, D.E., Traverse, A., Fensome, R.A. (2006). *The Triassic-Jurassic Fundy Basin, eastern Canada: regional setting, stratigraphy and hydrocarbon potential*. Atlantic Geology Vol. 32, Issue 3, pp 189-231.
- Waldron, J.W.F, Rosilli, C., Johnston, S.K., (2007). *Transpressional structures on a late Palaeozoic intracontinental transform fault, Canadian Appalachians*. Geological Society, London, Special Publications 2007; v. 290; p. 367-385.

Appendix A (John Thibodeau): Trim-shift SEG-Y program

The 'Trim-shift SEG-Y' program takes two files as input; the original SEG-Y formatted file, and a text file containing GPS coordinates of each trace found in the original data.

First, for each trace found in the original data file, the program computes the number of initial samples which comprise the lag time, by dividing the lag time by the sampling interval. Discarding the lag time samples effectively draws the interesting data up to the start of the trace.

Next, traces are topographically shifted to follow the terrain. Individual sample spacing is calculated by multiplying the sample interval by a velocity value, 0.1m/ns. GPS elevation data is then subtracted from a virtual "roof" set at 20m above sea-level. The elevation difference is then divided by the sample spacing to obtain the number of samples to prepend to the trace in order to shift the data downwards to the correct elevation.

Finally, all traces are padded to a pre-defined sample length, set at 300 samples, and a new, negative lag time is added to all traces to draw the data up to the 20m roof.

Since the original trace data is based on time, not depth, when loaded into the 3D processing software, all traces are visually displayed as starting at $Z=0$ ($t=0$) and extending downwards as time increases. Since we wanted the data to have an initially positive Z value in agreement with actual terrain elevation, a negative lag time was specified to pull the entire data set upwards into positive Z space. A value of 20m was chosen as the 'roof' since all elevation data is below 20m, so all data could then be 'hung' from 20m and extend downwards.

The bottom of each trace is padded to 300 samples so that, once topographically shifted, all traces have the same length.

CAVEAT: This program was written for this specific project. As such, proper formatting of input file is assumed (e.g. GPS coordinate files must contain one line for each trace coordinate.) No error checking is done. Also, certain values have been defined for this project, such as velocity, a virtual roof, and a desired trace height. This program could be made more general by first scanning the entire input file to determine appropriate values.

```

/* trimshiftsegy.c */
/* */
/* Program to trim lag time samples from SEG-Y data, apply GPS */
/* coordinates to traces, and add samples to topographically shift */
/* data. */
/* */
/* Written by: */
/* John Thibodeau <jthibo@dal.ca> */
/* Department of Earth Sciences */
/* Dalhousie University */
/* Halifax, Nova Scotia */
/* CANADA */

#include <stdio.h>

main ( int argc, char *argv[] ) {

    /* Structure to overlay header data. The */
    /* only binary header value we need is */
    /* the sample format (sample byte width). */
    struct header {
        unsigned char text[3200];
        struct {
            unsigned char skipa[24];
            short int sampleFormat;
            unsigned char skipb[374];
        } bin;
        unsigned short int sampleBytes;
    } header;

    /* Structure to overlay trace header data. */
    /* Only fields of interest are defined. */
    struct traceHeader {
        unsigned char skipa[40];
        int receiverElevation;
        int sourceSurfaceElevation;
        unsigned char skipb[20];
        short int elevationScalar;
        short int locationScalar;
        int sourceX;
        int sourceY;
        int groupX;
        int groupY;
        unsigned char skipc[16];
        short int lagA;
        unsigned char skipd[8];
        short int traceSamples;
        short int sampleInt;
        unsigned char unassigned[122];
        /* End of trace header. */
        long lagSampleBytes;
        unsigned int sampleDataSize;
        unsigned int topoPad;
    }

```

```

    unsigned int    sampleHeight;
    unsigned int    bottomPad;
} traceHeader;

int i, traceHeight = 300; /* Predefined trace height in samples to, */
                          /* allow samples to shift down to follow */
                          /* topography. */
float velocity = 0.01; /* Centimetres per picosecond. Yes cm/ps. */
                       /* GPR measures sample intervals is ps, */
                       /* and elev. units are in cm. */
int roof = 2000; /* False roof to hang survey from, in */
                /* centimetres above sea-level. */
unsigned char *traceData; /* Pointer for sample data. */
double gpsX, gpsY, gpsZ; /* Will hold read-in GPS values. */
unsigned char zeroByte = 0x00;
FILE *input; /* Original SEG-Y file. */
FILE *gpsFile; /* Prepared GPS data text file. */
FILE *output; /* Destination SEG-Y file. */

/* Program arguments are: */
/* <original.sgy> <gps.txt> <output.sgy> */
if ( argc == 4 ) {
    input = fopen ( argv[1], "rb" );
    gpsFile = fopen ( argv[2], "r" );
    output = fopen ( argv[3], "wb" );
} else {
    printf ( "Bad arguments!\n" );
    return 1;
}

/* Slurp in the text and binary header. */
fread ( &header, 1, 3600, input);

/* Convert sample format flag to a byte size. */
switch (header.bin.sampleFormat) {
    case 8:
        header.sampleBytes = 1;
        break;
    case 3:
        header.sampleBytes = 2;
        break;
    case 1: case 2: case 4: case 5:
        header.sampleBytes = 4;
        break;
}

/* Get space big enough to store sample data. */
traceData = (char*) malloc ( traceHeight * header.sampleBytes );

/* Write the untouched text and binary headers. */
fwrite ( &header, 1, 3600, output );

/* Loop while we can still read trace headers. */
while ( fread ( &traceHeader, 1, 240, input ) ) {

    /* Sample height is the velocity *times* the sample interval. */
    traceHeader.sampleHeight = velocity * traceHeader.sampleInt;

```

```

/* Original sample data size is the number of samples *times* the */
/* sample byte size. */
traceHeader.sampleDataSize = traceHeader.traceSamples
    * header.sampleBytes;

/* Bytes to skip over (lag bytes) is the lag time *divided* by */
/* the sample interval, *times* the sample byte size. */
traceHeader.lagSampleBytes = ( ( traceHeader.lagA * 1000 )
    / traceHeader.sampleInt ) * header.sampleBytes;

/* Skip over the lag bytes. */
fseek ( input, traceHeader.lagSampleBytes, SEEK_CUR );

/* Read in trace data. Size calculated by original sample size */
/* *minus* lag bytes. */
fread ( traceData, 1,
    traceHeader.sampleDataSize - traceHeader.lagSampleBytes,
    input );

/* Read a line of GPS. Field 3, 4, and 5 are X, Y, and elevation. */
fscanf ( gpsFile, "%i %f %lf %lf %lf %f", &gpsX, &gpsY, &gpsZ );

/* MODIFY TRACE HEADERS */
/* X,Y, and elev. are recorded in cm. These scalars will convert */
/* units back to metres. */
traceHeader.locationScalar = -100;
traceHeader.elevationScalar = -100;

/* Multiply all GPS values by 100 to convert from m to cm. */
traceHeader.sourceX = gpsX*100;
traceHeader.sourceY = gpsY*100;
traceHeader.sourceSurfaceElevation = gpsZ*100;
traceHeader.groupX = gpsX*100;
traceHeader.groupY = gpsY*100;
traceHeader.receiverElevation = gpsZ*100;

/* The number of samples to read is the original sample count, */
/* *minus*, start lag *divided* by the sample interval. */
traceHeader.traceSamples -= ( ( traceHeader.lagA * 1000 )
    / traceHeader.sampleInt );

/* Topographical padding is the false roof of the survey *minus* */
/* the elevation, *divided* by the height of one sample. */
traceHeader.topoPad = (roof - traceHeader.sourceSurfaceElevation)
    / traceHeader.sampleHeight;

/* Bottom padding rounds out the trace so that all traces in a */
/* line are equal depth. Bottom padding is the predefined trace */
/* height *minus* number of samples *minus* the topo. padding. */
traceHeader.bottomPad = ( traceHeight - traceHeader.traceSamples
    - traceHeader.topoPad );

/* Number of trace samples is now set to the predefined trace */
/* height. */
traceHeader.traceSamples = traceHeight;

/* Start lag is set to negative to drag the survey up to the */
/* false roof, in m. */

```

```

    traceHeader.lagA = 0 - ( roof / 100 );

    /* Write the new trace header. */
    fwrite ( &traceHeader, 1, 240, output );

    /* Write topographical pad samples. */
    for ( i = 0; i < traceHeader.topoPad * header.sampleBytes; i++ )
        fwrite ( &zeroByte, 1, 1, output );

    /* Write actual sample data. */
    fwrite ( traceData, 1,
            traceHeader.sampleDataSize - traceHeader.lagSampleBytes,
            output );

    /* Write bottom pad samples. */
    for ( i = 0; i < traceHeader.bottomPad * header.sampleBytes; i++ )
        fwrite ( &zeroByte, 1, 1, output );
}

fclose ( input );
fclose ( gpsFile );
fclose ( output );
}

```